Progress in Nuclear Magnetic Resonance Spectroscopy 134–135 (2023) 39–51

Contents lists available at ScienceDirect

Progress in Nuclear Magnetic Resonance Spectroscopy

journal homepage: www.elsevier.com/locate/pnmrs

Metabolic imaging with deuterium labeled substrates

Jacob Chen Ming Low, Alan J. Wright, Friederike Hesse, Jianbo Cao, Kevin M. Brindle *

Cancer Research UK Cambridge Institute, Li Ka Shing Centre, Robinson Way, Cambridge, CB2 0RE, UK

Handling Editor: David Neuhaus

ARTICLE INFO

Article history:
Received 6 January 2023
Accepted 7 February 2023
Available online 10 February 2023

Keywords:
Metabolism
Deuterium
Hyperpolarized-^{13}C
PET

ABSTRACT

Deuterium metabolic imaging (DMI) is an emerging clinically-applicable technique for the non-invasive investigation of tissue metabolism. The generally short T_1 values of ^{2}H-labeled metabolites *in vivo* can compensate for the relatively low sensitivity of detection by allowing rapid signal acquisition in the absence of significant signal saturation. Studies with deuterated substrates, including [6,6′-$^2H_2$]glucose, [$^2H_3$]acetate, [$^2H_9$]choline and [2,3-$^2H_2$]fumarate have demonstrated the considerable potential of DMI for imaging tissue metabolism and cell death *in vivo*. The technique is evaluated here in comparison with established metabolic imaging techniques, including PET measurements of 2-deoxy-2-[^{18}F]fluoro-D-glucose (FDG) uptake and ^{13}C MR imaging of the metabolism of hyperpolarized ^{13}C-labeled substrates.

Contents

Abbreviations: DMI, deuterium metabolic imaging; PET, positron emission tomography; ^{18}FDG, 2-deoxy-2-[^{18}F]fluoro-D-glucose; MRI, magnetic resonance imaging; MRS, magnetic resonance spectroscopy; PHIP, parahydrogen hydrogen-induced polarization; Glx, the unresolved deuterium resonances of C4-labeled glutamate and glutamine; CSI, chemical shift imaging; SNR, signal-to-noise ratio; TCA, tricarboxylic acid; LDH, lactate dehydrogenase; PDH, pyruvate dehydrogenase; ATP, adenosine triphosphate; PPP, pentose phosphate pathway; UV, ultraviolet; CEST, chemical exchange saturation transfer; ACSS1, acetyl-CoA synthetase 1; ACSS2, acetyl-CoA synthetase 2; ppm, parts per million; PCho, phosphocholine; CDP, cytidine diphosphate; NAD+, nicotinamide adenine dinucleotide; NADH, reduced form of nicotinamide adenine dinucleotide; *TERT*, Telomerase reverse transcriptase.

* Corresponding authors at: Cancer Research UK Cambridge Institute, Li Ka Shing Centre, Robinson Way, Cambridge, CB2 0RE, UK.

E-mail addresses: Jacob.Low@cruk.cam.ac.uk (J. Chen Ming Low), Alan.Wright@gstt.nhs.uk (A.J. Wright), Friederike.Hesse@cruk.cam.ac.uk (F. Hesse), Jianbo.Cao@cruk.cam.ac.uk (J. Cao), kmb1001@cam.ac.uk (K.M. Brindle).

https://doi.org/10.1016/j.pnmrs.2023.02.002
0079-6565/

1. Introduction

1.1. Clinical metabolic imaging

Metabolic imaging using MRI and PET is a powerful non-invasive technique for the clinical assessment of a range of pathologies, in particular cancer. In contrast to conventional anatomical imaging with CT and MRI, metabolic imaging is capable of detecting early changes in disease state that can precede morphological changes [1]. While proton MRS can provide a profile of the steady state concentrations of tissue metabolites [2], it lacks information about metabolic flux. Flux measurements using MRS have typically involved the administration of ^{13}C-labeled substrates and then monitoring ^{13}C label incorporation into downstream metabolites. These studies, which became popular in the 1980s [3], were eventually translated to the clinic where they were used, for example, to measure muscle glycogen synthesis following intravenous injection of [^{13}C]glucose [4]. However, lack of sensitivity, which results in poor temporal and spatial resolution, precluded widespread clinical adoption. More recently the sensitivity problem has been addressed by pre-polarizing the ^{13}C nuclear spins using dynamic nuclear polarization (DNP) [5] or parahydrogen-induced polarization (PHIP) techniques [6], which has led to much improved temporal and spatial resolutions. However, the complexity and cost of the DNP process coupled with the very short lifetime of the nuclear spin hyperpolarization (typically 2–3 min) has, at the present time, inhibited more widespread clinical application. The recent demonstration that ^{2}H MRI (DMI) could be used to follow the metabolism of [6,6′-$^{2}H_2$]glucose following oral administration in healthy normal volunteers and in cancer patients [7] has led to a resurgence of interest in this metabolic imaging technique, which was first described in the 1980s (reviewed in [8]).

1.2. ^{2}H as an isotope label for metabolic imaging

At first sight ^{2}H would appear to be an unpromising isotope label for probing tissue metabolism with magnetic resonance. The low gyromagnetic ratio (~6.5x lower than proton) and narrow spectral frequency range, coupled with broad resonances resulting from deuterium's nuclear quadrupolar moment, can lead to poorly resolved spectra that are detected with relatively low sensitivity. For example, the resonances of glutamate and glutamine labeled at the C4 position (also called C$^{\gamma}$) are not resolved and their intensities are typically reported as the sum for glutamate and glutamine (abbreviated as Glx) [7,9]. However, the generally short metabolite T_1 relaxation times means that the low sensitivity can be compensated by rapid signal acquisition, in the absence of significant signal saturation, and image resolutions have been obtained clinically in the brain that are comparable with those obtained for hyperpolarized ^{13}C-labeled lactate, albeit with a longer acquisition time and at a higher magnetic field [10,11]. The low natural abundance of the isotope (0.0115 %) means that apart from labeled water there are no background signals, which reduces spectral crowding. For example, there is little or no signal from lipids, which can hinder ^{1}H spectroscopy *in vivo*, and the natural abundance water resonance (which is equivalent to ~ 14 mM deuterium in tissue) provides an inbuilt concentration standard which, when correcting for saturation of the metabolite signals, allows signal intensities to be converted into absolute concentrations [8]. The T_1s of the deuterated metabolites of interest are mostly short but for some metabolites absolute quantification requires some correction for signal saturation. For example, for [6,6′-$^{2}H_2$]glucose, which has a T_1 of 50–70 ms *in vivo*, this is less of a problem than for [$^{2}H_3$]acetate, which has T_1 *in vivo* of over 2 s [12]. There has been some variation in the values used for the deuterium isotopic content of water in the DMI studies of metabolism published thus far, reflecting the fact that there is some variation in this value across the planet [8]. The metabolism of deuterium-labeled substrates will show a kinetic isotope effect if cleavage of a C—H bond, where the hydrogen is substituted for deuterium, is rate-limiting for the enzyme-catalyzed reaction. In general, however, kinetic isotope effects in enzyme-catalyzed reactions tend to be small and moreover would only affect metabolic flux *in vivo* if the enzyme had a high flux control coefficient for pathway flux. In metabolic pathways control tends to be distributed with no one enzyme controlling flux [13]. Studies in rat brain with glucose and acetate double labeled with ^{13}C and ^{2}H showed that kinetic isotope effects were very small [14].

1.3. Techniques for imaging the metabolism of ^{2}H-labeled substrates

Many of the initial studies imaging [6,6′-$^{2}H_2$]glucose metabolism used chemical shift imaging (CSI), often accompanied by the use of de-noising techniques to improve signal-to-noise ratios (SNR). Li et al [15] used extended k-space sampling and a machine learning approach to de-noising that produced images from rat brain tumors at 16.4 T with a nominal spatial resolution of 1.65 × 1.65 × 4.8 mm^3 and a temporal resolution of 0.9 – 1.8 min, an impressive 7-fold improvement in spatial resolution and 6-fold improvement in temporal resolution over a de-noising method used previously [16]. In addition to using de-noising techniques SNR can also be increased by acquiring signal at high magnetic fields and by using alternative pulse sequences to CSI. de Graaf et al. [17] showed that for the small surface coils used in animal studies the sensitivity scales with the magnetic field to a power of + 1.75, which is in agreement with theory if coil noise dominates, and for larger clinical surface coils as a + 1.65 power. At 9.4 T and using a double-tuned phased array coil with 10 transmit/receive channels for ^{1}H and 8 transmit/receive channels for ^{2}H Ruhm et al [10] used a CSI sequence to follow the metabolism of [6,6′-$^{2}H_2$]glucose to produce labeled Glx and water in the human brain with a temporal resolution of 10 min and a spatial resolution of 15 × 15.4 × 12.9 mm (voxel volume 2.97 mL). A similar study at 7 T achieved a nominal spatial resolution of 2.7 mL [18]. Peters et al. [19] combined a balanced steady state free precession sequence with IDEAL spectroscopic encoding to produce high resolution ^{2}H images of labeled water, glucose and lactate in orthotopic pancreatic tumor models in mice and showed that the sequence gave a threefold higher SNR for glucose and a twofold higher SNR for water than CSI. Incorporation of a DMI acquisition into a clinical protocol would inevitably add significantly to the time the patient was in the scanner if the ^{1}H and ^{2}H acquisitions were performed sequentially. Liu et al. [20] exploited the short repetition times used in DMI to interleave acquisition of the ^{2}H images within the delay periods in the proton sequence, thus acquiring the

^{1}H and ^{2}H images effectively simultaneously and without detriment to the quality of either image. Most clinical scanners are optimized for ^{1}H detection. Liu et al. got around this problem by using a custom-built hardware unit to up-convert the ^{2}H signals to ^{1}H frequencies so that only ^{1}H frequencies were sent to the scanner's receive path. Another solution to this problem is to detect ^{2}H incorporation into cell metabolites indirectly by monitoring the decrease in intensity of their proton resonances, a technique used over 40 years ago to detect lactate labeling from [$^{2}H_3$]pyruvate in erythrocyte suspensions [21]. Rich et al. [22] detected glutamate, glutamine and γ-aminobutyric acid labeling through decreases in their signal intensities in ^{1}H spectra acquired at 9.4 T from the brains of rats infused with [6,6′-$^{2}H_2$]glucose. In rats with orthotopically implanted gliomas they also detected lactate production in the tumors. The majority of the experiments employed single voxel proton spectroscopy although they also detected glutamate labeling in normal rat brain using ^{1}H CSI measurements. The group subsequently demonstrated this technique in normal human brain with proton CSI acquisitions at 7 T in subjects administered [6,6′-$^{2}H_2$]glucose orally [23].

We discuss in the following the ^{2}H-labeled substrates that have been described to date, how they can be used with DMI to probe various aspects of tissue metabolism and how they compare with the same or similar substrates that have been labeled with PET-detectable radionuclides or ^{13}C MR-detectable hyperpolarized ^{13}C labels.

2. Imaging glucose metabolism

2.1. Imaging with ^{2}H-labeled glucose

The most widely used substrate to date has been [6,6′-$^{2}H_2$]glucose, whose metabolism in the glycolytic pathway results, in some tissues, in detectable labeling of the lactate methyl group, with entry of methyl group-labeled pyruvate into the mitochondrial tricarboxylic acid (TCA) cycle resulting in labeling of the TCA cycle intermediate, α-ketoglutarate, at the C4 position. Labeled α-ketoglutarate exchanges its C4 deuterium label with glutamate, which can also be converted into glutamine, resulting in labeling of both glutamate and glutamine at their C4 positions (Glx) (Fig. 1 A&B).

Glx labeling provides a detectable surrogate for α-ketoglutarate labeling and therefore for TCA cycle flux. The relationship between [6,6′-$^{2}H_2$]glucose consumption and lactate production is not stoichiometric since the deuterium label can be lost to solvent water in several enzyme catalyzed reactions, including that catalyzed by pyruvate kinase, and via Schiff base formation with cell amino groups [24]. Some of the ^{2}H label that enters the TCA cycle via pyruvate is also lost to solvent water in the reactions catalyzed by aconitase and isocitrate dehydrogenase before the remaining label appears in α-ketoglutarate. Glucose labeled at the C1 position also gives rise to labeled lactate and Glx, although some of this label at the C1 position is lost to the pentose phosphate pathway

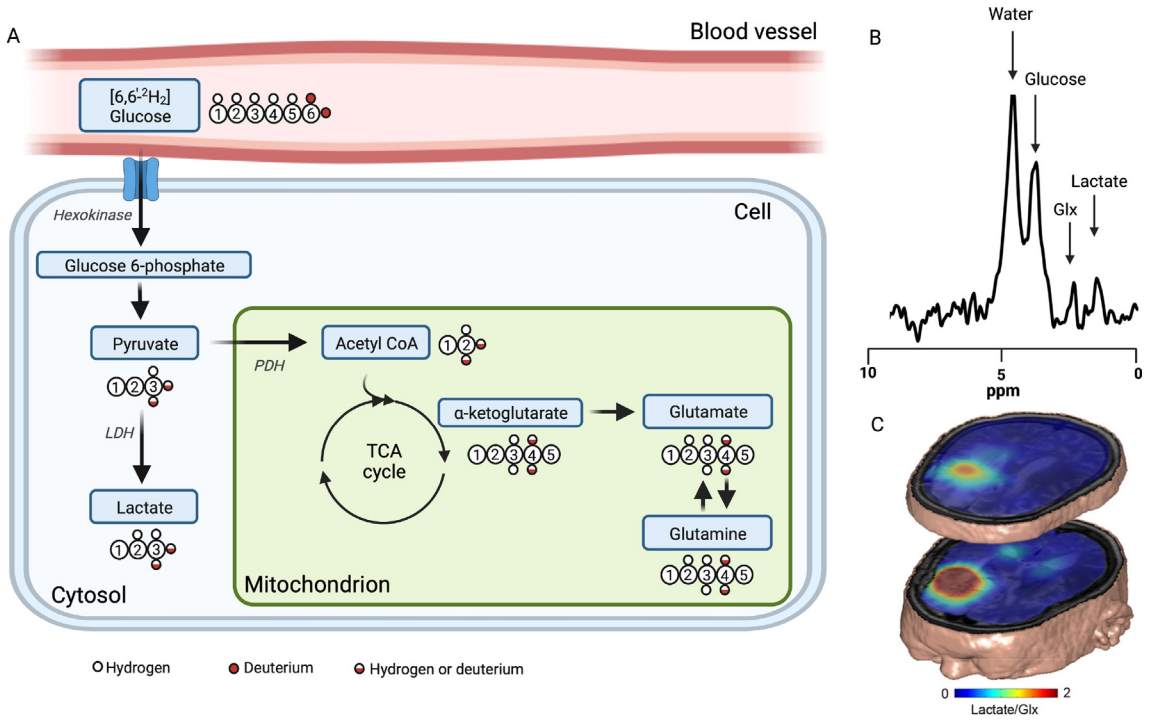

Fig. 1. Deuterated glucose metabolism. (A) Glucose is delivered via the blood stream and enters the cell via the glucose transporters where it is phosphorylated to produce glucose 6-phosphate (G6P) in the reaction catalysed by hexokinase, the first enzyme in the glycolytic pathway. G6P is then metabolized through a series of reactions to produce pyruvate, which is then either reduced to produce lactate, catalysed by lactate dehydrogenase (LDH), or converted into acetyl-CoA by the mitochondrial pyruvate dehydrogenase (PDH) complex. Acetyl-CoA then enters the TCA cycle where it undergoes a series of oxidation reactions that lead ultimately to the generation of ATP and TCA cycle intermediates that serve as the starting point for various biosynthetic reactions. α-ketoglutarate, one of these intermediates, is in rapid exchange with glutamate, in the reaction catalysed by glutamate-pyruvate transaminase. Glutamate can be converted, in an irreversible reaction catalysed by glutamine synthetase, to produce glutamine, which can be broken down to glutamate in another irreversible reaction catalysed by glutaminase. The labeling patterns in pyruvate, lactate, α-ketoglutarate, glutamate and glutamine are described in [8]. **(B)** Representative ^{2}H spectrum acquired from the brain of a mouse with an orthotopically implanted patient-derived glioblastoma xenograft following intravenous administration of 2 g/kg [6,6′-$^{2}H_2$]glucose (unpublished data). **(C)** Maps of the labeled lactate/Glx ratio following oral administration of [6,6′-$^{2}H_2$] glucose to a glioblastoma patient. The ratio is markedly increased in the tumour, reflecting increased glycolytic metabolism when compared to normal brain tissue. (Image reproduced with permission from [7]).

(PPP) and also through phosphomannose isomerase activity [8]. Deuterium labels at the C2-C5 positions in glucose are all lost to solvent water in the glycolytic pathway and therefore using [U-$^2H_7$]-glucose as the labeled substrate results in substantially more water labeling. However, using the ^2H signal from labeled water as a surrogate for imaging glycolytic and TCA cycle activities is compromised *in vivo* by wash-in of labeled water from other tissues [16]. Nevertheless, this approach has been used in rats infused with [U-$^2H_7$]-glucose to image cerebral metabolism by imaging the water labeling that occurred in a pseudo-steady state obtained prior to wash-in of labeled water from peripheral tissues [25]. Label loss to solvent water will likely be a problem for other ^2H-labeled substrates and can reduce sensitivity. For example, the hydration of [2,3-$^2H_2$]fumarate to produce labeled malate in the reaction catalyzed by fumarase has been used to detect tumor cell necrosis *in vivo* [26]. However, ^2H label in malate can be lost to solvent water through exchange with oxaloacetate, in the reaction catalyzed by malate dehydrogenase, and subsequent keto-enol tautomerization of the oxaloacetate.

The current resurgence in interest in ^2H MRSI as a metabolic imaging technique can be traced back to two papers published in 2017 and 2018, in which ^2H MR was used to monitor brain [6,6′-$^2H_2$]glucose metabolism. Chen and colleagues used ^2H MRS at 16.4 T to measure cerebral glucose and Glx labeling in rats infused with [6,6′-$^2H_2$]glucose and demonstrated greater neuronal activity (increased cerebral glucose consumption and TCA cycle flux) under morphine as compared to isoflurane anesthesia [9]. de Graaf and colleagues used a pulse-acquire sequence with 3D phase-encoding gradients following the excitation pulse to map the metabolism of [6,6′-$^2H_2$]glucose and [$^2H_3$]acetate in rat brain at 11.7 T, where they observed labeling of lactate, in the case of glucose infusion, and Glx labeling following both glucose and acetate infusion at 1.95 g/kg and 2 g/kg respectively [7]. In liver they observed labeling of glycogen following [6,6′-$^2H_2$]glucose infusion and in the brains of rats implanted with a glioma model they observed increased lactate labeling and decreased Glx labeling in the tumor compared to surrounding normal brain tissue, reflecting the increased glycolytic and decreased oxidative metabolism of the tumor. These brain images were acquired over 35 min with a nominal spatial resolution of $2 \times 2 \times 2$ mm^3. This was a landmark paper since these authors also showed increased lactate labeling and decreased Glx labeling, compared to normal brain tissue, in the tumors of glioma patients in images acquired at 4 T between 65 and 90 min following oral administration of [6,6′-$^2H_2$]glucose (0.6 g/kg body weight) (Fig. 1C). The nominal image resolution in this case was $20 \times 20 \times 20$ mm. By trading resolution for a decreased acquisition time, in part by employing a weighted k-space acquisition, Kreis et al. [16] acquired 3D images at 9.4 T and used these to measure the rates of glucose consumption and labeled lactate production in a subcutaneous murine lymphoma model. A series of 5 images was acquired over a period of 50 min with a nominal spatial resolution of $3 \times 3 \times 9$ mm^3. Fitting of these data to a model of the glycolytic pathway enabled calculation of tumor glycolytic flux maps in mM/min, which showed a dramatic decrease in tumor glycolytic flux by 24 h after treatment of the animals with a chemotherapeutic drug (Fig. 2).

A tensor de-noising technique was used to improve quantification of the signals in this highly correlated multi-dimensional data set. A similar low-rank de-noising was employed by von Morze et al. in a study of [6,6′-$^2H_2$]glucose metabolism in the rat brain at 4.7 T [27] (Fig. 3).

Simoes et al [28] used localized ^2H spectroscopy measurements of [6,6′-$^2H_2$]glucose metabolism at 9.4 T and a PCA-based approach to de-noising to show that glucose oxidation (Glx labeling) in orthotopically implanted glioblastoma allografts in immunocompetent mice was correlated with cell proliferation, regardless of the metabolic characteristics of the glioblastoma model. Increased glycolytic flux, relative to normal brain, was observed in the tumors of mice implanted orthotopically with human astrocytes using ^2H MRS measurements at 14.1 T of labeled lactate production from [6,6′-$^2H_2$]glucose [29]. The increased flux was attributed to elevated expression of the glycolytic enzyme phosphofructokinase-1. Treatment of the animals with a poly(ADP-ribose) polymerase (PARP) inhibitor resulted in a decrease in labeled lactate production before there was any change in tumor size. Standard-of-care treatment for glioblastoma involves surgical resection followed by targeted radiation of the resection cavity. However, it is difficult using current MRI techniques to distinguish recurrent tumor from radiation-induced necrosis. Using a mouse model in which glioblastoma cells were implanted in irradiated brain tissue Ge et al. showed, using single voxel ^2H spectroscopy in mice infused with $\sim$ 2 g/kg [6,6′-$^2H_2$]glucose, that tumor tissue shows a higher lactate/Glx signal ratio compared to radiation necrosis, which displays a ratio that is more similar to normal brain [30]. In mice implanted orthotopi-

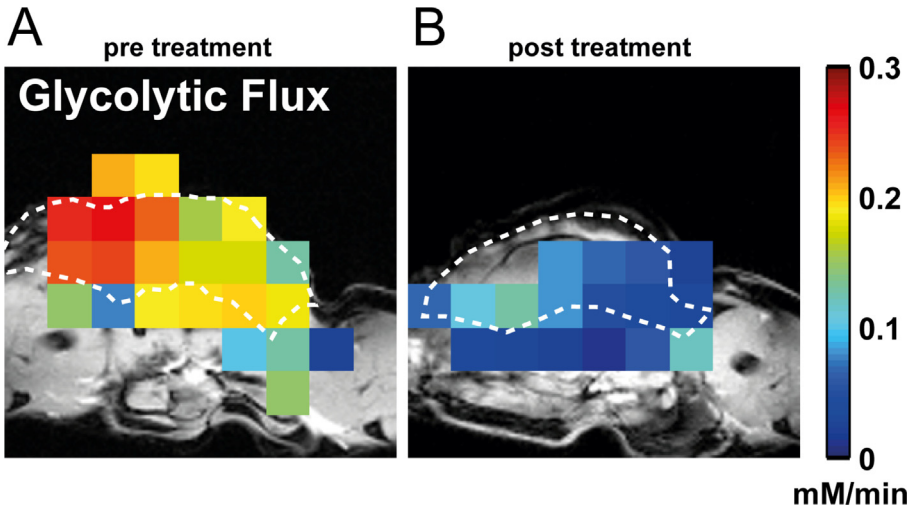

Fig. 2. Imaging tumor glycolytic flux. A series of ^2H 3D chemical shift images was obtained from a tumor-bearing mouse following intravenous administration of [6,6′-$^2H_2$]glucose before and after treatment. The glucose and lactate signal intensities were fit to a model of the glycolytic pathway and used to produce maps of glycolytic flux in mM/min. Maps of tumor glycolytic flux before **(A)** and after **(B)** treatment overlaid on gray scale ^1H images of tissue anatomy. (Figure reproduced with permission from [16]).

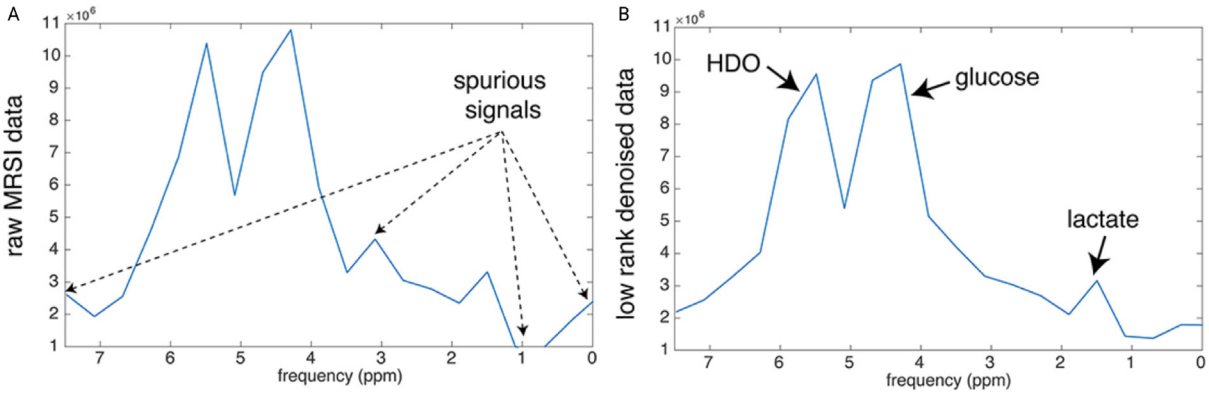

Fig. 3. Effect of de-noising on ^{2}H spectra. Spectra processed with **(A)** and without **(B)** de-noising. (Figure reproduced with permission from [27]).

cally with pancreatic tumor models and injected with [6,6′-$^{2}H_2$]glucose, labeled lactate was observed in tumors that were greater than 5 mm in diameter. Labeled water was observed throughout the abdomen of the animals but in higher concentrations in the tumor and in the kidney and bladder [31].

^{2}H imaging of glucose metabolism has also been used in other disease settings and to study metabolism in other tissues. In a rat stroke model, which employed unilateral occlusion of the middle cerebral artery, increased lactate labeling and decreased Glx labeling was observed in and around the ischemic lesion [32]. Images were acquired at 9.4 T with a resolution of $3 \times 3 \times 3$ mm^3. The increase in lactate labeling and decrease in Glx reflects the expected increase in anaerobic glycolysis and decrease in oxidative metabolism respectively. Using a closed-chest rat model, in which a surface coil was placed directly over the heart, Glx labeling was observed to be faster in animals infused with [2,2,2-$^{2}H_3$]acetate than with [6,6′-$^{2}H_2$]glucose, consistent with previous studies showing that the heart prefers acetate over glucose as a substrate [12]. In these healthy hearts, labeled lactate production from [6,6′-$^{2}H_2$]glucose was very low or undetectable although it could be expected to be increased following an infarct. Preeclampsia in pregnancy is a condition characterized by high-blood pressure that can lead to organ damage in developing fetuses and an increase in anaerobic metabolism. Using a vasoconstrictor that produces symptoms in a mouse model that mimic preeclampsia, glucose uptake and labeled lactate production were shown to be higher in the placenta and fetuses of preeclamptic animals injected with [6,6′-$^{2}H_2$]glucose [33]. Slice-selective chemical shift images were acquired at 15.1 T using a surface coil in $\sim$ 8 min with a slice thickness of 4–8 mm and a nominal in plane resolution of $\sim 5 \times 5$ mm^2. Activation of brown adipose tissue (BAT) results in increased energy expenditure and heat generation due to mitochondrial uncoupling mediated by uncoupling protein 1 (UCP1) and as a consequence has become a target for treatments that combat obesity. DMI was used to assess glucose metabolism in the BAT tissue of cold-adapted rats by placing a surface coil over the neck and shoulder regions that contain BAT and acquiring slice-selective chemical shift images at 9.4 T from a 10 mm thick slice with a nominal in plane resolution of 5×5 mm^2 [34]. The glucose signal was 2.4 and 1.4-fold higher at 20 and 40 min after glucose infusion and the labeled water signal higher at 60 min in the BAT of the cold-acclimatized rats when compared to controls.

2.2. Imaging with hyperpolarized ^{13}C-labeled glucose

Glucose metabolism can also be imaged using hyperpolarized ^{13}C-labeled glucose by extending the relatively short ^{13}C polarization lifetime through deuteration. Per-deuteration of uniformly ^{13}C-labeled glucose ([U-$^{2}H_7$, U-^{13}C] D-glucose) extended the T_1 for the combined ^{13}C resonances at 9.4 T to $\sim$ 9 s, which was sufficiently long to image flux through all 11 steps in the glycolytic pathway, from glucose to lactate, in a subcutaneous murine lymphoma model *in vivo* [35]. Labeled 6-phosphogluconate, an intermediate in the PPP, was also observed and therefore the experiment also gave an indication of PPP activity and thus the capacity of the tumor to resist oxidative stress [36,37]. Coil-localized ^{13}C spectra from mice implanted orthotopically with human glioblastoma cells and injected with [U-$^{2}H_7$, U-$^{13}C_6$]glucose showed that a glioblastoma subtype that formed compact hypoxic tumors showed higher levels of lactate labeling when compared to the contralateral hemisphere and the brains of control animals whereas tumor models that were representative of the invasive edge of the tumor showed lower levels of lactate labeling, reflecting a less glycolytic phenotype [38]. Cell proliferation is accompanied by the shortening of telomeres, which are structures at the end of chromosomes that protect them from damage. Most cancers maintain telomere length, which enables sustained proliferation, by reactivating telomerase reverse transcriptase (*TERT*) expression. In orthotopically implanted tumor models of low-grade oligodendrogliomas *TERT* expression was shown to be associated with increased PPP activity, which could be detected through ^{13}C MRS and MRSI measurements of increased 6PG concentrations following injection of hyperpolarized [U-$^{2}H_7$, U-$^{13}C_6$]glucose. Evidence was presented that *TERT* increased PPP flux by upregulating expression of the glucose transporter, GLUT1, and the PPP enzyme, glucose 6-phosphate dehydrogenase [39].

While experiments with hyperpolarized ^{13}C-labeled glucose have shown promise in these preclinical experiments, these measurements would be difficult to translate to the clinic because of the relatively short T_1 ($\sim$14 s at 3 T) of the labeled glucose. Increased levels of polarization and the use of glucose isotopomers that eliminate ^{13}C–^{13}C spin coupling would improve sensitivity. The sensitivity of glycolytic flux measurements in a brain tumor model were increased by using [2,3,4,6,6′-$^{2}H_5$, 3,4-$^{13}C_2$]glucose, which removes ^{13}C–^{13}C coupling in the 3 carbon intermediates in the pathway and in the resulting lactate [40]. A recent study achieved 70 % polarization of [U-$^{2}H_7$, U-^{13}C]glucose [41] as compared to $\sim$ 15 % in the first study that used this molecule [35], although it is still not clear that this would be sufficient for clinical studies. A further limitation of the hyperpolarized ^{13}C experiment, in its current form, is that because of the short polarization lifetime an expensive and relatively complex hyperpolarization device must be placed immediately adjacent to the MRI scanner. This requirement could be relaxed if the hyperpolarized ^{13}C-labeled material could be produced centrally and shipped to the scanner. The development of UV-induced radicals, which can substitute

for the stable radicals that are normally used in the DNP process, allows for this possibility since they can be thermally annihilated, without substantial loss of nuclear spin polarization, and allow the hyperpolarized ^{13}C-labeled compound to be stored at low temperature and in a strong magnetic field [42]. The radiology department would then only need a device for rapidly heating the stored polarized material to room temperature for injection. As well as not requiring complex equipment for its production, ^{2}H-labeled glucose can be used to follow the metabolism of glucose over much longer periods of time, which means that it measures something different to the hyperpolarized ^{13}C experiment. In a study in mouse brain, ^{1}H spectra showed a significantly higher lactate concentration in animals anesthetized with isoflurane compared to those anesthetized with a combination of medetomidine and isoflurane. Infusion of [6,6′-$^{2}H_2$]glucose resulted in lactate labeling in animals anesthetized with isoflurane but not in animals anesthetized with a combination of medetomidine and isoflurane whereas in animals infused with hyperpolarized [$^{2}H_7$, U-$^{13}C_6$]glucose lactate labeling was detected under both anesthetic conditions. The labeled lactate/glucose signal ratio was also higher in this latter group, indicating that there was increased conversion of hyperpolarized ^{13}C-labeled glucose into lactate. Modelling showed that fractional ^{13}C labeling of the lactate pool was low at between 6 and 25 % and therefore what dominated lactate labeling in this case was influx of hyperpolarized ^{13}C label into the lactate pool rather than its efflux and that lactate pool size will have little effect on the observed labeling. Contrast this with the experiment with [6,6′-$^{2}H_2$] D-glucose where lactate labeling was measured over a much longer period of time (~1 h) where the labeling rate is inversely proportional to lactate pool size and when a steady state is reached the concentration of ^{2}H-labeled lactate will be proportional to that observed in the ^{1}H MR experiment [43].

2.3. Imaging with thermally polarized ^{13}C-labeled glucose

The de-noising techniques that have been used with ^{2}H-labeled glucose have also been used with thermally polarized ^{13}C-labeled glucose. Kishimoto et al achieved an approximately 30-fold improvement in signal-to-noise ratio by using low rank tensor decomposition and showed that imaging with non-hyperpolarized [U-^{13}C]glucose could distinguish between different subtypes of pancreatic cancer when implanted as subcutaneous xenografts [44]. Images acquired at 9.4 T with a spatial resolution of 0.3 cm × 0.3 cm × 1.5 cm showed similar glucose uptake rates in the two subtypes but differences in glucose utilization. Imaging the metabolism of hyperpolarized [1-^{13}C]pyruvate could not distinguish between the two subtypes and the absence of any differences in glucose uptake suggest that ^{18}FDG-PET would also be unable to distinguish between them.

2.4. Imaging with unlabeled glucose

Delivery of glucose to a tissue and its uptake can also be detected using chemical exchange saturation transfer (CEST), where the glucose is detected by saturating the resonances of the glucose hydroxyl protons and monitoring the decrease in intensity of the signal from the water protons, with which they are in exchange [45]. The technique has the advantage that it does not require labeling of the glucose molecule but there appears to be no evidence that it can detect any downstream glucose metabolism.

2.5. Imaging with PET and [^{18}F] fluoro-2-deoxyglucose

PET detection of the uptake and trapping of the radioactive glucose analogue, [^{18}F] fluoro-2-deoxyglucose (^{18}FDG), has been used widely in the clinic to stage tumors and monitor treatment response in several malignancies [1]. Despite its widespread use the technique has several limitations. The radiation involved precludes its use in children and women of childbearing age and in pathologies that require multiple investigations for long-term follow up. Detection of tumors in the brain and prostate is compromised in the former by high uptake in normal brain tissue and in the latter by renal clearance of ^{18}FDG and its accumulation in the adjacent bladder. Moreover, the technique only assesses flux in the first three steps of tissue glucose metabolism, these being delivery via the circulation, uptake on the glucose transporters and subsequent phosphorylation and trapping in the reaction catalyzed by the first enzyme in the glycolytic pathway, hexokinase [46] (Fig. 1 A). This may make it insensitive to some perturbations that affect glycolytic flux. For example, in a study on colorectal xenografts treated with a TRAIL agonist, which induces rapid tumor cell death, there was no change in ^{18}FDG uptake but a dramatic decrease in the conversion of thermally polarized ^{13}C-labeled glucose to lactate [47].

3. Imaging metabolism with other ^{2}H-labeled substrates

3.1. 3-O-methylglucose

3-O-methylglucose (OMG) is a glucose analog that has been used, in ^{11}C-labeled form, to study glucose transport in skeletal muscle using PET [48], and in unlabeled form to study tumor perfusion and glucose uptake in breast cancer models using CEST [49]. The methyl group has also been deuterated and wash in and wash out of the labeled molecule in a subcutaneous breast cancer metastasis model in the rat has been studied using ^{2}H MRS and 2D ^{2}H CSI measurements [50]. Spectra and images were acquired at 7 T using a surface coil placed over the tumor following intravenous injection of 0.89 g/kg OMG. Images were acquired with a nominal spatial resolution of 7.1 × 7.1 × 7.9 mm^3 and spectra with a temporal resolution of 5 s.

3.2. Acetate

Infusion of [$^{2}H_3$]acetate into rats with an orthotopically implanted glioma model showed increased acetate uptake and reduced Glx labeling in the tumor when compared to surrounding normal brain tissue (Fig. 4). Infusion of [6,6′-$^{2}H_2$]glucose showed reduced Glx labeling in the tumor and increased lactate labeling [7]. Both experiments indicated reduced TCA cycle activity in the tumor with the increased lactate labeling showing increased glycolytic activity.

In a study in rat heart, infusion of [$^{2}H_3$]acetate resulted in a higher rate of increase in the labeled water peak and a peak assigned to Glx when compared to animals infused with [6,6′-$^{2}H_2$] D-glucose, consistent with the heart's preference, under normal conditions, to consume fatty acids or acetate instead of glucose [12]. 3D CSI images were acquired at 16.4 T using a surface coil placed under the chest muscle. The nominal voxel volume was 0.44 mL and therefore the myocardial tissue volume was covered by 2–3 CSI voxels.

3.2.1. Imaging with ^{13}C- and ^{11}C-labeled acetate

Acetate metabolism in normal rat brain has been studied using thermally polarized [2-^{13}C]acetate, where the labeled acetate and fractional labeling of glutamate and glutamine at the C3 and C4 positions were detected indirectly via the spin-coupled proton resonances in localized ^{1}H spectra (resolution: 8 × 3 × 6 mm^3) acquired from the cerebral cortex at 14.1 T [51]. Acetate is metabolized within the brain almost exclusively in glial cells and these

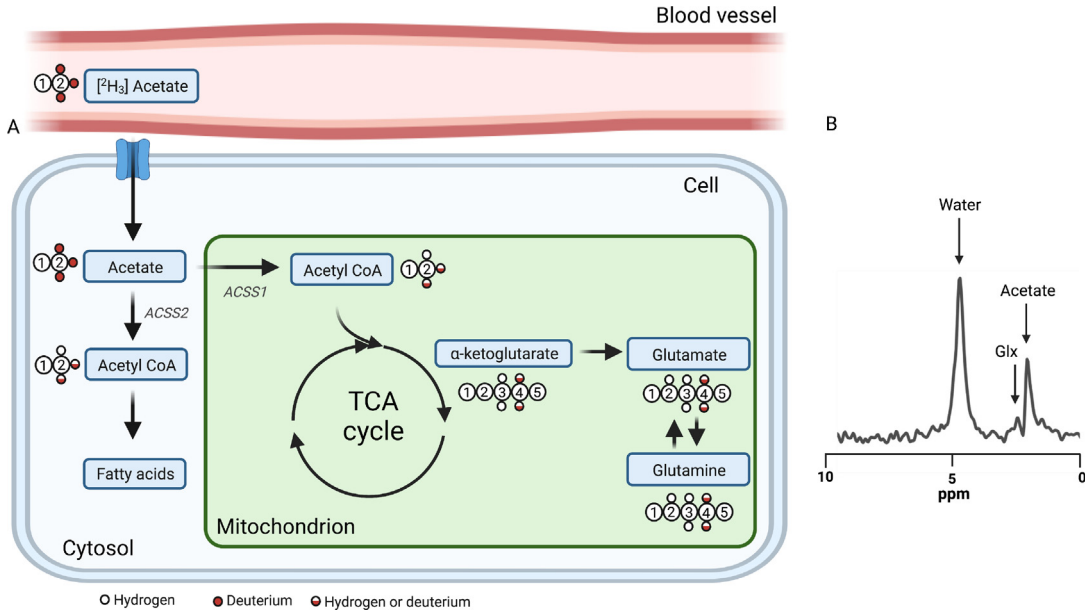

Fig. 4. Metabolism of deuterated acetate. (A) Acetate is taken up into the cell by the monocarboxylate transporters and is converted to acetyl CoA by acetyl-CoA synthetase 1 (ACSS1) in the mitochondria, and by ACSS2 in the cytosol. Acetyl CoA in the mitochondria enters the TCA cycle whereas acetyl CoA in the cytosol can be used in fatty acid synthesis. (**B)** Representative spectrum obtained from the brain of a rat with an orthotopically implanted patient-derived glioblastoma xenograft following intravenous administration of 2 g/kg [$^2H_3$]acetate (unpublished data). Glutamate and glutamine (Glx) are labeled via α-ketoglutarate in the TCA cycle. The labeling patterns in α-ketoglutarate, glutamate and glutamine are described in [8].

measurements gave an estimate of glial cell TCA cycle rate. Acetate metabolism has also been studied in normal brain and in brain tumors using PET measurements of ^{11}C-acetate uptake. Acetate uptake in glioblastoma is greater than surrounding normal brain tissue and the contrast observed is greater than that observed with ^{18}FDG. Furthermore, acetate uptake increases with tumor grade, whereas ^{18}FDG uptake is unable to distinguish between tumors of different grade (reviewed in [52]). The ^{11}C label in acetate is incorporated into TCA cycle intermediates and at later times into lipids (Fig. 4). Studies with [1-^{11}C], [1-^{13}C], and [1-^{14}C]acetate in prostate and lung cancer models showed that, in order to detect incorporation of [1-^{11}C]acetate into lipid, PET scans should be acquired later than 30 min after injection, which will result in a significant loss of SNR due to the short half-life of the isotope (20.4 min) [53]. There appear to be no DMI studies as yet that have demonstrated incorporation of [$^2H_3$]acetate into lipid; however a very early study demonstrated incorporation of ^{2}H into lipids in mice given ^2H_2O in their drinking water [54].

TCA cycle activity has been estimated in the rat heart using hyperpolarized [1-^{13}C]acetate. Localized ^{13}C spectra were acquired with a 3 s time resolution using a surface coil placed over the chest. Label incorporation into [1-^{13}C]acetylcarnitine and into the TCA cycle intermediate [5-^{13}C]citrate was observed and used to estimate TCA cycle flux [55]. The [1-^{13}C]acetyl carnitine resonance was much more intense than the [5-^{13}C]citrate resonance and in animals infused with [1-^{13}C]butyrate more intense than the [5-^{13}C]glutamate resonance [56]. The [5-^{13}C]glutamate resonance is obscured in animals infused with hyperpolarized [1-^{13}C]acetate by the acetate resonance. Since ^{1}H chemical shifts for the C4 resonances of glutamate lie between 2.1 and 2.2 ppm and that for the acetyl group in acetyl carnitine is at 2.13 ppm [57], and given the similarity between ^{1}H and ^{2}H chemical shifts, it seems likely that the peak assigned to Glx in the animals infused with [$^2H_3$]acetate could contain a significant contribution from ^{2}H-labeled acetyl carnitine. In humans cardiac PET measurements of [1-^{11}C]acetate uptake has been used to provide a quantitative assessment of myocardial perfusion and oxidative metabolism with a spatial resolution of ~ 1 cm [58].

3.3. Choline

^{1}H and ^{31}P MR studies have shown elevated levels of choline metabolites in tumors, reflecting the need for increased membrane biosynthesis in rapidly proliferating tumor cells [59] (Fig. 5A). In breast cancer cells the increased phosphocholine concentration was shown to be due to increased expression of choline kinase and in lung cancer patients increased expression of choline kinase has been correlated with relapse-free and overall survival. In an early study, choline metabolism was investigated in human breast cancer xenografts by infusing tumor-bearing mice with [$^2H_9$]-choline at 16 μmol/kg/min for 2 h and acquiring ^{2}H spectra at 4.7 T from a 1 cm^3 tumor voxel [60]. Between 40 and 60 min after the start of infusion there was a gradual increase in a peak at 3.2 ppm, which was assigned to choline, phosphocholine and betaine. In a more recent study, mice with subcutaneous human renal carcinoma xenografts were infused with [$^2H_9$]choline (0.05 g/kg), either alone or with [6,6′-$^2H_2$]glucose (1.3 g/kg), and ^{2}H 3D chemical shift images were acquired at 11.7 T at high resolution (nominally 2 × 2 × 2 mm^3) in 37 min or at low resolution (nominally 3.7 × 3.7 × 3.7 mm^3) in 2.24 min. Broadening of the tumor choline resonance over time was attributed to the production of choline metabolites [61] (Fig. 5B). In both studies, atropine was injected to prevent a cholinergic reaction to the choline bolus. High resolution ^{2}H spectra of tumour extracts from rats with orthotopically implanted glioblastomas and infused with [1,1,2,2-$^2H_4$]choline showed resolvable resonances from choline, phosphocholine and glycerophosphorylcholine [62].

3.3.1. Imaging with ^{13}C-, ^{11}C- and ^{15}N-labeled choline

Both hyperpolarized ^{13}C- and ^{15}N-labeled choline have been investigated *in vivo*. Hyperpolarized [^{15}N]choline has a T_1 *in vitro* of ~ 4 min; however the chemical shift separation of the choline and phosphocholine peaks is only ~ 0.2 ppm, which would make [^{15}N]phosphocholine difficult to detect *in vivo* [63]. Surface coil-localized ^{15}N spectra were obtained from the heads of rats infused with 2.5 mL of ~ 90 mM hyperpolarized [^{15}N]choline, where the solid-state polarization was ~ 3 % [64]. Measurements of relax-

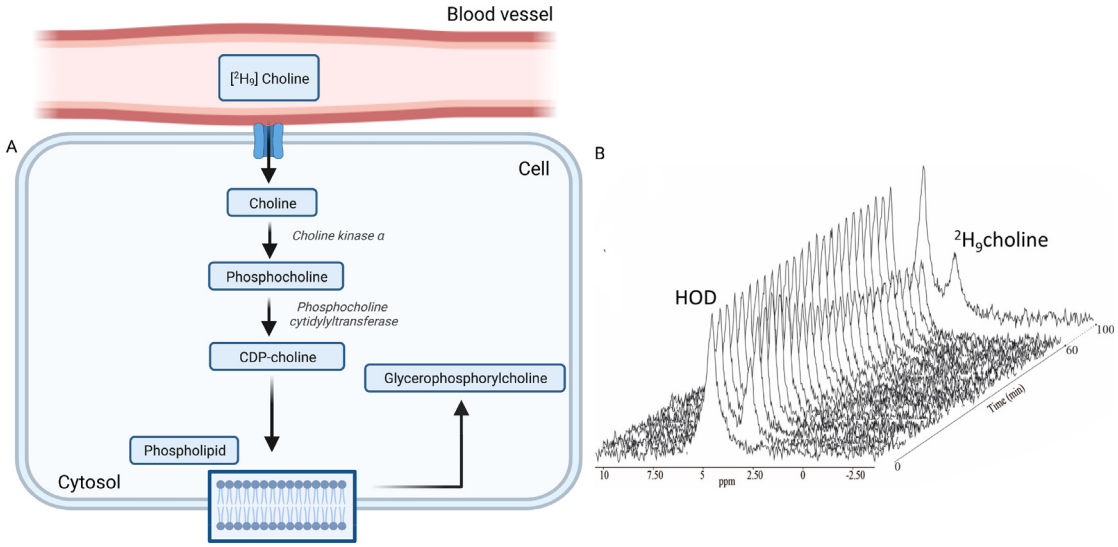

Fig. 5. Choline metabolism. (A) Choline is taken up into cells by choline transporter-like protein 1 (CTL1) and phosphorylated to produce phosphocholine (PCho) by choline kinase α. PCho is converted to CDP-choline by phosphocholine cytidylyltransferase, which is then used in phospholipid synthesis. Glycerophosphorylcholine is produced through phospholipid breakdown. **(B)** ^{2}H spectra acquired using a surface coil from a subcutaneous tumour in a mouse infused with 0.05 g/kg [$^{2}H_9$]choline. (Figure reproduced with permission from [61]).

ation times *in vivo* showed biexponential behavior, with a fast decay during the first few seconds and then a slower relaxation thereafter, which was interpreted as coming from choline first in the blood pool and then subsequently in the brain. Projection images (nominal resolution 3.1 × 3.1 mm) were acquired using a volume coil from rats infused with 2.5 mL of 12.6, 25, or 50 mg/kg hyperpolarized [1,1,2,2-$^{2}H_4$, 1-^{13}C]choline chloride [65]. Deuteration extends the ^{13}C polarization lifetime and in this study at 3 T the T_1 in solution was 30 s. There was no attempt to image the metabolism of the labeled choline, only its distribution over time. PET measurements of [^{11}C]choline uptake have been used to image various cancers, including tumors in the brain [66] and prostate [67]. In breast cancer patients [^{11}C]choline uptake was ~ 10x lower in normal breast and lung tissues when compared to the tumors, where uptake was higher in the more aggressive tumors [68].

3.4. Pyruvate

The expression of *TERT*, which maintains telomere length, is increased in cancer cells and is a marker of cell proliferation. In patient-derived models of glioblastoma increased *TERT* expression was shown to drive increased expression of nicotinamide phosphoribosyl transferase, which is involved in NAD + biosynthesis, and the glycolytic enzyme glyceraldehyde-3-phosphate dehydrogenase, which catalyzes the reduction of NAD + to NADH. ^{2}H 2D CSI images acquired at 14.1 T from mice with orthotopically implanted patient-derived glioblastoma xenografts and injected with 0.45 g/kg [U-^{2}H]-pyruvate showed increased production of labeled lactate in the tumor, when compared to adjacent brain tissue. The nominal in plane resolution was 3.75 mm^2. Treatment of the animals with a *TERT* inhibitor resulted in a substantial decrease in lactate labeling before there was any decrease in tumor volume [69].

3.4.1. Imaging with hyperpolarized ^{13}C-labeled pyruvate

Flux in the reaction catalyzed by LDH (see Fig. 1) has also been studied using hyperpolarized [1-^{13}C]pyruvate. From early preclinical studies on imaging tumor grade and treatment response and cardiac metabolism (reviewed in [70–72]) the technique progressed to the first clinical study in prostate cancer [73] and subsequently to clinical studies in brain [74,75] and heart [76,77] and in tumors of the breast [78,79], brain [80–83,84] and kidney [85], with further studies in prostate cancer [86,87] (reviewed in [88,89]). Exchange of isotope label (^{2}H or hyperpolarized ^{13}C) between the injected labeled pyruvate and the endogenous lactate pool depends on delivery of pyruvate to the tissue, uptake of pyruvate on the monocarboxylate transporters and subsequent exchange of label between pyruvate and lactate catalyzed by lactate dehydrogenase (LDH) (Fig. 1). The exchange catalyzed by LDH is very sensitive to the NADH concentration, increasing with increases in the concentration of the reduced coenzyme [90]. Increased lactate labeling in tumors and decreases post-treatment has been a general observation in tumor-bearing animals and patients injected with hyperpolarized [1-^{13}C]pyruvate [72,91], although increases in lactate labeling have also been observed following treatment [79]. In principle [U-^{2}H]-pyruvate could be used in the same way that hyperpolarized [1-^{13}C]pyruvate has; however the administered dose of ^{13}C-labeled pyruvate is considerably lower than for the ^{2}H-labeled molecule. For the patient studies a typical hyperpolarized [1-^{13}C]pyruvate dose is 0.4 mL/kg body weight of an approximately 250 mM solution, which equates to ~ 9 mg/kg as compared to 0.45 g/kg used in the preclinical [U-^{2}H]-pyruvate studies [69].

von Morze et al [27] compared spectroscopic imaging with hyperpolarized [1-^{13}C]pyruvate and with [6,6′-$^{2}H_2$]glucose in the rat brain at 4.7 T. Dual tuned ^{13}C/^{1}H and ^{2}H/^{1}H surface coils were constructed that had similar dimensions and had similar sensitivity for ^{2}H and ^{13}C detection, a consequence of the opposite effects of the smaller gyromagnetic ratio of ^{2}H but the greater magnetic moment of this quadrupolar nucleus. The animals were infused with 1 g/kg [6,6′-$^{2}H_2$]glucose and separately with 40 mg/kg [1-^{13}C]pyruvate and 2D CSI images acquired with a 4 × 4 mm^2 nominal resolution for ^{13}C and 8 × 8 mm^2 for ^{2}H. The ^{13}C images showed signal from lactate, demonstrating that there is a lactate pool in the brain that can exchange ^{13}C label with the injected pyruvate and that is indicative of glycolytic activity. However, there was no signal from ^{13}C-labeled bicarbonate, which is produced in the irreversible reaction catalyzed by mitochondrial pyruvate dehydrogenase and is a measure of TCA cycle activity and oxidative metabolism (Fig. 1), although labeled bicarbonate has

been observed previously in the brain following hyperpolarized [1-^{13}C]pyruvate administration in preclinical [92] and clinical studies [74,93]. The ^{2}H images showed signal from labeled glucose, lactate, and Glx. The SNR for the pyruvate ^{13}C signal was ~ 10x that of the glucose ^{2}H signal and the SNR of the lactate ^{13}C signal was ~ 5x that of the lactate ^{2}H signal. The failure to detect ^{13}C-labeled bicarbonate, which involves just one step in the TCA cycle, but detection of ^{2}H-labeled Glx, which involves several, presumably reflects the more limited time over which labeled CO_2 and bicarbonate can accumulate before there is complete loss of the polarization, which is relatively fast in CO_2 and bicarbonate. There was, nevertheless, an inverse linear correlation between ^{2}H labeling of Glx and ^{13}C labeling of lactate which would be expected if pyruvate is diverted away from reduction to lactate towards oxidation in the TCA cycle.

3.5. Fumarate

Fumarate, an intermediate in the tricarboxylic acid cycle, is hydrated in the reaction catalyzed by the intracellular enzyme fumarase to produce malate. In most viable cells exogenous fumarate is taken up relatively slowly; however in necrosis fumarate rapidly gains access to intracellular fumarase via a leaky plasma membrane, either inside the cell or outside the cell, resulting in a substantial increase in malate production (Fig. 6).

Fumarase has no coenzyme requirement and only requires water as a co-substrate, and therefore in principle is active outside the cell as well as inside. Moreover, it has a high specific activity and a low K_M for fumarate making it a very sensitive sensor of necrotic cell death. This was first exploited as a method for detecting cell death using hyperpolarized [2,4-^{13}C]fumarate. Treatment of murine lymphoma-bearing mice with a chemotherapeutic drug resulted in a substantial increase, compared to baseline, of labeled malate in the tumor following intravenous injection of hyperpolarized [1,4-$^{13}C_2$]fumarate [95]. The technique has also been used to detect cell death in other tumor models [96,97] and in models of myocardial infarction [98] and acute kidney necrosis [99]. As cell death is detected by an increase in the malate/fumarate signal ratio it corrects for any changes in tissue perfusion, and as the technique produces positive contrast and can integrate signal over a large volume it is capable of detecting relatively low levels of diffuse tissue necrosis that cannot be detected using diffusion-weighted ^{1}H MRI [97]. The same experiment can be performed using [2,3-$^{2}H_2$]fumarate as the ^{2}H resonances of fumarate and malate

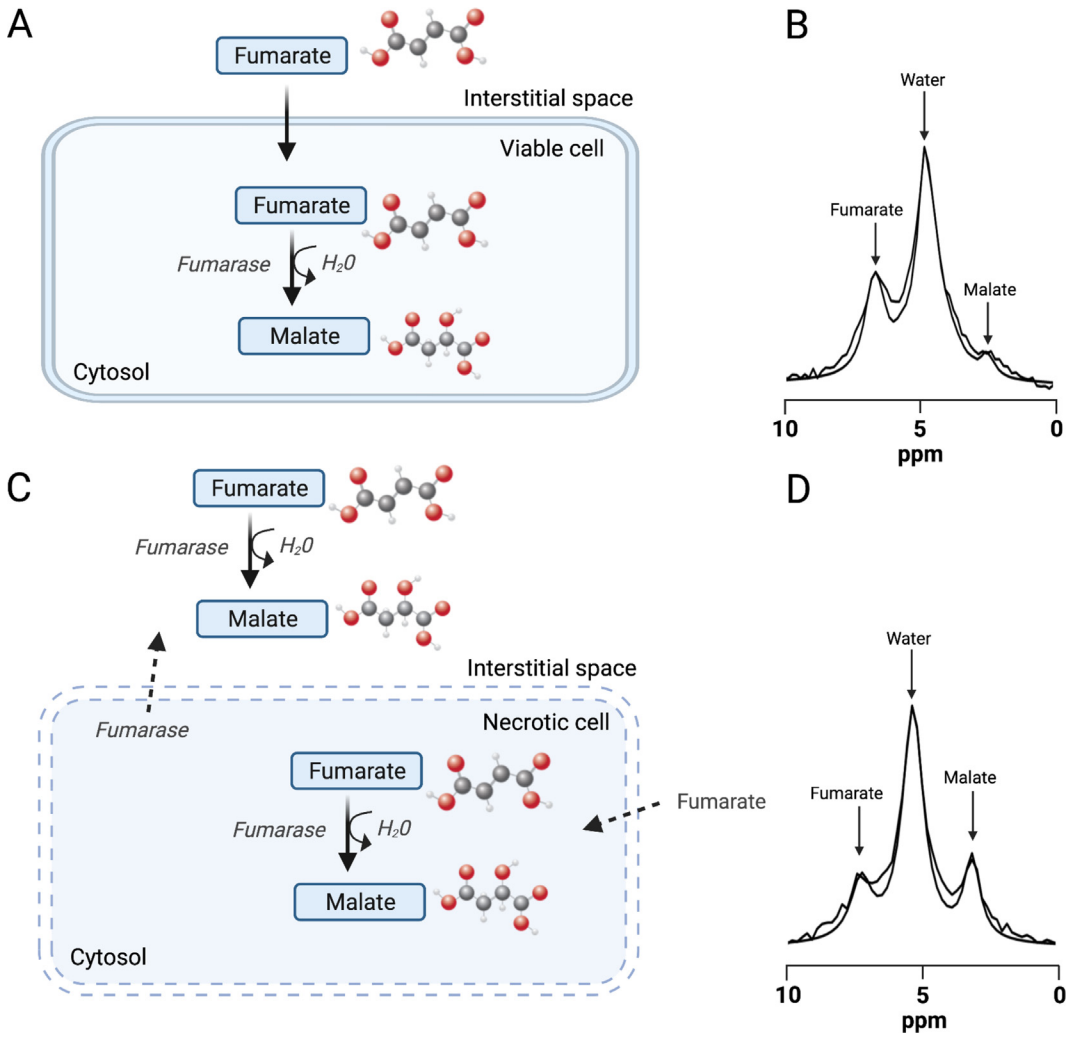

Fig. 6. Deuterated fumarate metabolism in viable and necrotic cells. **A**) In viable cells fumarate enters the cells slowly and there is little production of labeled malate. (**B**) Representative ^{2}H spectrum acquired from the brain of an untreated mouse with an orthotopically implanted patient-derived glioblastoma xenograft following administration of 1 g/kg body weight [2,3-$^{2}H_2$] disodium fumarate injected intravenously. (**C**) In necrotic cells fumarate rapidly gains access to fumarase via the permeabilized plasma membrane. (**D**) Representative ^{2}H spectrum acquired from a patient-derived glioblastoma xenograft following treatment with chemoradiation. Note the marked increase in labeled malate. (Panels B & D reproduced with permission from [94]).

are well resolved from each other and from the water resonance [26] (Fig. 6B&D). Initial experiments with [2,3-$^{2}H_2$]fumarate were used to measure treatment-induced cell death in two human xenograft models and in the murine lymphoma model (EL4) used for the original experiments with hyperpolarized [1,4-$^{13}C_2$]fumarate [95]. Although the malate SNR in ^{2}H MR spectra of EL4 tumors (2.9 ± 0.2) was much lower than the SNR of ^{13}C-labeled malate following the administration of hyperpolarized [1,4-$^{13}C_2$]fumarate (~17) the ^{2}H MRS measurements appear to provide a more sensitive method for detecting cell death as they show much greater image contrast. Following hyperpolarized [1,4-$^{13}C_2$]fumarate injection, the [1,4-^{13}C]malate/[1,4-^{13}C]fumarate ratio increased by a factor of ~ 1.6 following treatment, as compared to an increase by a factor of ~ 10 in the ^{2}H-labeled malate/fumarate ratio after [2,3-$^{2}H_2$]fumarate administration. This is a reflection of the much longer acquisition period over which malate production was measured in the ^{2}H experiments, 65 min as compared to 3 min in the case of the hyperpolarized ^{13}C experiments. ^{2}H-labeled fumarate has also been used to assess cell death in two orthotopically implanted patient-derived xenografts and in a human cell-line model of glioblastoma at 48 h following the completion of targeted chemo-radiotherapy [94]. 3D chemical shift images, with a nominal resolution of 3 × 3 × 9 mm^3, were acquired following intravenous infusion over 20 min of 1 g/kg body weight [2,3-$^{2}H_2$] disodium fumarate, and metabolite maps were produced from images summed over the first 30 min of signal acquisition. The malate/fumarate signal ratio increased by nearly a factor of 10 in the most radiosensitive tumor, whereas in animals injected with the hyperpolarized [1,4-$^{13}C_2$]fumarate the ratio increased by only 1.6-fold and did not reach statistical significance. The increase in the malate/fumarate signal ratio was also a more sensitive indicator of treatment response than either diffusion-weighted or contrast agent-enhanced ^{1}H MRI measurements, which are amongst the techniques used currently to detect glioblastoma response to chemo-radiotherapy in the clinic. The concentrations of fumarate and malate detected in these tumors, which are comparable to the concentrations of glucose, lactate and Glx measured in clinical studies, coupled with the relatively large chemical shift separation of the fumarate, malate and water resonances suggest that this technique for detecting glioblastoma cell death could in principle translate to the clinic. In the murine lymphoma model oral administration of fumarate gave as much tumor fumarate and malate signal as that obtained following intravenous fumarate administration [100]. Since fumarate has been given to patients at doses of up to 30 g [101], apparently without toxic effects, then there appears to be no toxicity barrier in translating this technique to the clinic.

4. Conclusions

Since the first clinical study in 2018 [7], DMI has rapidly established itself as a powerful technique for metabolic imaging that has considerable clinical potential, particularly in the field of oncology where it could be used both to predict which treatment will be most effective in a tumor subtype and then subsequently to detect early evidence of treatment response. The technique can thus be used to spare the patient the toxic effects of an ineffectual treatment and allow rapid selection of a more effective therapy [1]. The most obvious rival to this technology is ^{13}C MRSI with hyperpolarized ^{13}C-labeled cell substrates, which has also translated to the clinic. DMI has the advantage that ^{2}H-labeled substrates can be taken off the shelf and administered without the complex and expensive equipment required to hyperpolarize ^{13}C-labeled substrates and does not require the logistical set-up for rapid injection and fast imaging necessitated by the short half-life of ^{13}C hyperpolarization. ^{2}H-labeled substrates are in general cheaper to produce than ^{13}C-labeled substrates (10 g of [6,6′-$^{2}H_2$]glucose cost $791 as compared to 10 g of [1-^{13}C]glucose, which cost $1,259 from Cambridge Isotopes in December 2022. Five g of [1-^{13}C]pyruvic acid cost $2,854) but this advantage is offset by the much larger amounts of ^{2}H-labeled substrates that are needed for clinical studies, which also carries with it potential toxicity issues (~50 g of [6,6-$^{2}H_2$]glucose for a 70 kg patient as compared to 1.5 g of [1-^{13}C]pyruvic acid [78]). Toxicity has not been a problem for studies with ^{2}H-labeled glucose but may be a problem for other ^{2}H-labeled substrates that could be developed for clinical translation in the future, although this potential problem may be ameliorated to some extent by the possibility of oral administration. The much lower sensitivity of ^{2}H detection when compared to hyperpolarized ^{13}C is offset by the capacity to acquire signal for longer periods of time and ^{2}H images with resolutions similar to those of hyperpolarized ^{13}C images have been obtained. The capability to acquire images over longer periods of time can also increase image contrast, as was the case with [2,3-$^{2}H_2$]fumarate. Since imaging with ^{2}H– and hyperpolarized ^{13}C-labeled substrates can be used to image similar aspects of metabolism a key question is which has the greater potential for clinical application, or are they complementary? von Morz et al [27] sought to address this question in rat brain by comparing directly ^{13}C MRSI with hyperpolarized [1-^{13}C]pyruvate with DMI with [6,6′-$^{2}H_2$]glucose and concluded that they have significant potential to image specific segments of glucose metabolism.

The majority of preclinical DMI studies have been conducted at high magnetic fields, both to improve sensitivity and spectral resolution. However, acquiring preclinical data at clinical magnetic field strengths is not a prerequisite to demonstrate clinical translatability since coil configurations, relaxation times and voxel volumes may be very different between the two scenarios. Instead, it should be sufficient to show merely that the concentrations of deuterated metabolites detected in preclinical investigations are within the range of concentrations (1 – 5 mM) already detected in clinical studies.

Glucose has rapidly become an established substrate for DMI studies and one can anticipate that there will be exploration of further ^{2}H-labeled substrates in the coming years, much as occurred over the last 20 years for hyperpolarized ^{13}C-labeled substrates. In selecting labeled substrates that would be suitable for imaging metabolism with DMI it is important to choose substrates that will give rise to metabolites with resonances that are sufficiently well resolved from those of the substrate at clinical magnetic field strengths (typically 3 T) [93]. This will be aided by the chemical equivalence of ^{1}H and ^{2}H, which means that there is a wealth of proton NMR data that can be used to estimate ^{2}H chemical shifts. Metabolic imaging with hyperpolarized ^{13}C-labeled substrates has been limited to relatively fast metabolic reactions because of the short lifetime of the hyperpolarization and it might be assumed that this requirement could be relaxed with ^{2}H-labeled substrates. This appears to be the case with [$^{2}H_9$]choline where choline metabolites accumulate over a prolonged period of time. However, relatively fast metabolism may still be a requirement for substrates such as ^{2}H-labeled glucose and fumarate in order that their metabolites can accumulate to the millimolar concentrations required for detection.

For imaging with hyperpolarized ^{13}C-labeled substrates there was a period of 10 years between the first demonstration of the technique [5] and its first application in the clinic [73]. During this period there was very active preclinical exploration of the technology in the expectation, but not the certainty, that the technique would translate to the clinic. DMI starts from a point where clinical feasibility has already been demonstrated, which should stimulate its further preclinical and clinical exploration in the coming years.

Data availability

No data was used for the research described in the article.

Declaration of Competing Interest

The authors declare that they have no known competing financial interests or personal relationships that could have appeared to influence the work reported in this paper.

Acknowledgements

Work in KMB's laboratory that is related to the content of this review is funded by Cancer Research UK (Grant/Award Numbers: C197/A17242, C197/A16465, C9685/A25177) and by the European Union's Horizon 2020 Research and Innovation Program under FETOPEN grant agreement no.858149 (AlternativesToGd). J.C.M.L was supported by a clinical research training fellowship from the Medical Research Council UK (Grant Number: MR/V029452/1). The graphical abstract and Figs. 1, 4, 5 and 6 were created using BioRender.com.

References

[1] K. Brindle, New approaches for imaging tumour responses to treatment, Nat. Rev. Cancer 8 (2008) 94–107.
[2] M. Wilson, O. Andronesi, P.B. Barker, R. Bartha, A. Bizzi, P.J. Bolan, K.M. Brindle, I.Y. Choi, C. Cudalbu, U. Dydak, U.E. Emir, R.G. Gonzalez, S. Gruber, R. Gruetter, R.K. Gupta, A. Heerschap, A. Henning, H.P. Hetherington, P.S. Huppi, R.E. Hurd, K. Kantarci, R.A. Kauppinen, D.W.J. Klomp, R. Kreis, M.J. Kruiskamp, M.O. Leach, A.P. Lin, P.R. Luijten, M. Marjańska, A.A. Maudsley, D.J. Meyerhoff, C.E. Mountford, P.G. Mullins, J.B. Murdoch, S.J. Nelson, R. Noeske, G. Öz, J.W. Pan, A.C. Peet, H. Poptani, S. Posse, E.M. Ratai, N. Salibi, T.W.J. Scheenen, I.C.P. Smith, B.J. Soher, I. Tkáč, D.B. Vigneron, F.A. Howe, Methodological consensus on clinical proton MRS of the brain: Review and recommendations, Magn. Reson. Med. 82 (2019) 527–550.
[3] R.G. Shulman, D.L. Rothman, C-13 NMR of intermediary metabolism: Implications for systemic physiology, Annu. Rev. Physiol. 63 (2001) 15–48.
[4] G.I. Shulman, D.L. Rothman, T. Jue, P. Stein, R.A. Defronzo, R.G. Shulman, Quantitation of muscle glycogen-synthesis in normal subjects and subjects with non-insulin-dependent diabetes by C-13 nuclear magnetic-resonance spectroscopy, N. Engl. J. Med. 322 (1990) 223–228.
[5] J.H. Ardenkjaer-Larsen, B. Fridlund, A. Gram, G. Hansson, L. Hansson, M.H. Lerche, R. Servin, M. Thaning, K. Golman, Increase in signal-to-noise ratio of > 10,000 times in liquid-state NMR, Proc. Natl. Acad. Sci. USA 100 (2003) 10158–10163.
[6] J.B. Hovener, A.N. Pravdivtsev, B. Kidd, C.R. Bowers, S. Gloggler, K.V. Kovtunov, M. Plaumann, R. Katz-Brull, K. Buckenmaier, A. Jerschow, F. Reineri, T. Theis, R. V. Shchepin, S. Wagner, P. Bhattacharya, N.M. Zacharias, E.Y. Chekmenev, Parahydrogen-Based Hyperpolarization for Biomedicine, Angew. Chem.-Int. Ed. 57 (2018) 11140–11162.
[7] H.M. De Feyter, K.L. Behar, Z.A. Corbin, R.K. Fulbright, P.B. Brown, S. McIntyre, T.W. Nixon, D.L. Rothman, R.A. de Graaf, Deuterium metabolic imaging (DMI) for MRI-based 3D mapping of metabolism *in vivo*, Sci. Adv. 4 (2018) eaat7314.
[8] H.M. De Feyter, R.A. de Graaf, Deuterium metabolic imaging - Back to the future, J. Magn. Reson. 326 (2021).
[9] M. Lu, X.H. Zhu, Y. Zhang, G. Mateescu, W. Chen, Quantitative assessment of brain glucose metabolic rates using *in vivo* deuterium magnetic resonance spectroscopy, J. Cereb. Blood Flow Metab. 37 (2017) 3518–3530.
[10] L. Ruhm, N. Avdievich, T. Ziegs, A.M. Nagel, H.M. De Feyter, R.A. de Graaf, A. Henning, Deuterium metabolic imaging in the human brain at 9.4 Tesla with high spatial and temporal resolution, Neuroimage 244 (2021).
[11] J.W. Gordon, H.Y. Chen, A. Autry, I. Park, M. Van Criekinge, D. Mammoli, E. Milshteyn, R. Bok, D. Xu, Y. Li, R. Aggarwal, S. Chang, J.B. Slater, M. Ferrone, S. Nelson, J. Kurhanewicz, P.E.Z. Larson, D.B. Vigneron, Translation of Carbon-13 EPI for hyperpolarized MR molecular imaging of prostate and brain cancer patients, Magn. Reson. Med. 81 (2019) 2702–2709.
[12] T. Wang, X.H. Zhu, H. Li, Y. Zhang, W. Zhu, H.M. Wiesner, W. Chen, Noninvasive assessment of myocardial energy metabolism and dynamics using *in vivo* deuterium MRS imaging, Magn. Reson. Med. 86 (2021) 2899–2909.
[13] D.A. Fell, Metabolic control analysis: a survey of its theoretical and experimental development, Biochem. J. 286 (Pt 2) (1992) 313–330.
[14] R.A. de Graaf, M.A. Thomas, K.L. Behar, H.M. De Feyter, Characterization of Kinetic Isotope Effects and Label Loss in Deuterium-Based Isotopic Labeling Studies, ACS Chem. Nerosci. 12 (2021) 234–243.
[15] Y. Li, Y. Zhao, R. Guo, T. Wang, Y. Zhang, M. Chrostek, W.C. Low, X.H. Zhu, Z.P. Liang, W. Chen, Machine Learning-Enabled High-Resolution Dynamic Deuterium MR Spectroscopic Imaging, IEEE Trans. Med. Imag. 40 (2021) 3879–3890.
[16] F. Kreis, A.J. Wright, F. Hesse, M. Fala, D.-E. Hu, K.M. Brindle, Measuring Tumor Glycolytic Flux *in Vivo* by Using Fast Deuterium MRI, Radiology 294 (2020) 289–296.
[17] R.A. de Graaf, A.D. Hendriks, D.W.J. Klomp, C. Kumaragamage, D. Welting, C.S. Arteaga de Castro, P.B. Brown, S. McIntyre, T.W. Nixon, J.J. Prompers, H.M. De Feyter, On the magnetic field dependence of deuterium metabolic imaging, NMR Biomed. 33 (2020) e4235.
[18] E. Serés Roig, H.M. De Feyter, T.W. Nixon, L. Ruhm, A.V. Nikulin, K. Scheffler, N.I. Avdievich, A. Henning, R.A. de Graaf, Deuterium metabolic imaging of the human brain *in vivo* at 7 T, Magn. Reson. Med. 89 (2023) 29–39.
[19] D.C. Peters, S. Markovic, Q. Bao, D. Preise, K. Sasson, L. Agemy, A. Scherz, L. Frydman, Improving deuterium metabolic imaging (DMI) signal-to-noise ratio by spectroscopic multi-echo bSSFP: A pancreatic cancer investigation, Magn. Reson. Med. 86 (2021) 2604–2617.
[20] Y. Liu, H.M. De Feyter, R.K. Fulbright, S. McIntyre, T.W. Nixon, R.A. de Graaf, Interleaved fluid-attenuated inversion recovery (FLAIR) MRI and deuterium metabolic imaging (DMI) on human brain *in vivo*, Magn. Reson. Med. 88 (2022) 28–37.
[21] R.J. Simpson, K.M. Brindle, F.F. Brown, I.D. Campbell, D.L. Foxall, A p.m.r. isotope-exchange method for studying the kinetic properties of dehydrogenases in intact cells, Biochem. J. 202 (1982) 573–579.
[22] L.J. Rich, P. Bagga, N.E. Wilson, M.D. Schnall, J.A. Detre, M. Haris, R. Reddy, ^{1}H magnetic resonance spectroscopy of ^{2}H-to-^{1}H exchange quantifies the dynamics of cellular metabolism *in vivo*, Nat. Biomed. Eng. 4 (2020) 335–342.
[23] A.T.J. Cember, N.E. Wilson, L.J. Rich, P. Bagga, R.P.R. Nanga, S. Swago, A. Swain, D. Thakuri, M. Elliot, M.D. Schnall, J.A. Detre, R. Reddy, Integrating ^{1}H MRS and deuterium labeled glucose for mapping the dynamics of neural metabolism in humans, Neuroimage 251 (2022).
[24] R.J. Simpson, K.M. Brindle, F.F. Brown, I.D. Campbell, D.L. Foxall, Studies of pyruvate-water isotope exchange catalysed by erythrocytes and proteins, Biochem J 193 (1981) 401–406.
[25] R. Mahar, H. Zeng, A. Giacalone, M. Ragavan, T.H. Mareci, M.E. Merritt, Deuterated water imaging of the rat brain following metabolism of [$^{2}H_{7}$] glucose, Magn. Reson. Med. 85 (2021) 3049–3059.
[26] F. Hesse, V. Somai, F. Kreis, F. Bulat, A.J. Wright, K.M. Brindle, Monitoring tumor cell death in murine tumor models using deuterium magnetic resonance spectroscopy and spectroscopic imaging, Proc Natl Acad Sci U S A 118 (2021).
[27] C. von Morze, J.A. Engelbach, T. Blazey, J.D. Quirk, G.D. Reed, J.E. Ippolito, J.R. Garbow, Comparison of hyperpolarized ^{13}C and non-hyperpolarized deuterium MRI approaches for imaging cerebral glucose metabolism at 4.7 T, Magn Reson Med 85 (2021) 1795–1804.
[28] R.V. Simões, R.N. Henriques, B.M. Cardoso, F.F. Fernandes, T. Carvalho, N. Shemesh, Glucose fluxes in glycolytic and oxidative pathways detected *in vivo* by deuterium magnetic resonance spectroscopy reflect proliferation in mouse glioblastoma, Neuroimage Clin 33 (2022).
[29] C. Taglang, G. Batsios, J. Mukherjee, M. Tran, A.M. Gillespie, D. Hong, S.M. Ronen, H. Artee Luchman, R.O. Pieper, P. Viswanath, Deuterium magnetic resonance spectroscopy enables noninvasive metabolic imaging of tumor burden and response to therapy in low-grade gliomas, Neuro Oncol 24 (2022) 1101–1112.
[30] X. Ge, K.H. Song, J.A. Engelbach, L. Yuan, F. Gao, S. Dahiya, K.M. Rich, J.J.H. Ackerman, J.R. Garbow, Distinguishing Tumor Admixed in a Radiation Necrosis (RN) Background: ^{1}H and ^{2}H MR With a Novel Mouse Brain-Tumor/RN Model, Front Oncol 12 (2022).
[31] S. Markovic, T. Roussel, L. Agemy, K. Sasson, D. Preise, A. Scherz, L. Frydman, Deuterium MRSI characterizations of glucose metabolism in orthotopic pancreatic cancer mouse models, NMR Biomed 34 (2021) e4569.
[32] M. Straathof, A.E. Meerwaldt, H.M. De Feyter, R.A. de Graaf, R.M. Dijkhuizen, Deuterium Metabolic Imaging of the Healthy and Diseased Brain, Neuroscience 474 (2021) 94–99.
[33] S. Markovic, T. Roussel, M. Neeman, L. Frydman, Deuterium Magnetic Resonance Imaging and the Discrimination of Fetoplacental Metabolism in Normal and L-NAME-Induced Preeclamptic Mice, Metabolites 11 (2021) 376.
[34] M.J. Riis-Vestergaard, C. Laustsen, C. Mariager, R.F. Schulte, S.B. Pedersen, B. Richelsen, Glucose metabolism in brown adipose tissue determined by deuterium metabolic imaging in rats, Int J Obes (Lond) 44 (2020) 1417–1427.
[35] T.B. Rodrigues, E.M. Serrao, B.W. Kennedy, D.E. Hu, M.I. Kettunen, K.M. Brindle, Magnetic resonance imaging of tumor glycolysis using hyperpolarized ^{13}C-labeled glucose, Nat Med 20 (2014) 93–97.
[36] K.N. Timm, J. Hartl, M.A. Keller, D.-E. Hu, M.I. Kettunen, T.B. Rodrigues, M. Ralser, K.M. Brindle, Hyperpolarized [U-^{2}H, U-^{13}C]Glucose reports on glycolytic and pentose phosphate pathway activity in EL4 tumors and glycolytic activity in yeast cells, Magn. Reson. Med. 74 (2015) 1543–1547.
[37] K.N. Timm, D.E. Hu, M. Williams, A.J. Wright, M.I. Kettunen, B.W.C. Kennedy, T.J. Larkin, P. Dzien, I. Marco-Rius, S.E. Bohndiek, K.M. Brindle, Assessing Oxidative Stress in Tumors by Measuring the Rate of Hyperpolarized [1-^{13}C] Dehydroascorbic Acid Reduction Using ^{13}C Magnetic Resonance Spectroscopy, J Biol Chem 292 (2017) 1737–1748.
[38] M. Mishkovsky, O. Gusyatiner, B. Lanz, C. Cudalbu, I. Vassallo, M.F. Hamou, J. Bloch, A. Comment, R. Gruetter, M.E. Hegi, Hyperpolarized C-13-glucose magnetic resonance highlights reduced aerobic glycolysis *in vivo* in infiltrative glioblastoma, Sci. Rep. 11 (2021) 5771.

[39] P. Viswanath, G. Batsios, V. Ayyappan, C. Taglang, A.M. Gillespie, P.E.Z. Larson, H.A. Luchman, J.F. Costello, R.O. Pieper, S.M. Ronen, Metabolic imaging detects elevated glucose flux through the pentose phosphate pathway associated with TERT expression in low-grade gliomas, Neuro Oncol 23 (2021) 1509–1522.
[40] M. Mishkovsky, B. Anderson, M. Karlsson, M.H. Lerche, A.D. Sherry, R. Gruetter, Z. Kovacs, A. Comment, Measuring glucose cerebral metabolism in the healthy mouse using hyperpolarized C-13 magnetic resonance, Sci. Rep. 7 (2017) 11719.
[41] A. Capozzi, S. Patel, W.T. Wenckebach, M. Karlsson, M.H. Lerche, J.H. Ardenkjær-Larsen, Gadolinium Effect at High-Magnetic-Field DNP: 70% ^{13}C Polarization of [U-^{13}C] Glucose Using Trityl, J Phys Chem Lett 10 (2019) 3420–3425.
[42] A. Capozzi, T. Cheng, G. Boero, C. Roussel, A. Comment, Thermal annihilation of photo-induced radicals following dynamic nuclear polarization to produce transportable frozen hyperpolarized ^{13}C-substrates, Nat. Commun. 8 (2017) 15757.
[43] E. Flatt, B. Lanz, Y. Pilloud, A. Capozzi, M.H. Lerche, R. Gruetter, M. Mishkovsky, Measuring Glycolytic Activity with Hyperpolarized [$^{2}H_{7}$, U-$^{13}C_{6}$] D-Glucose in the Naive Mouse Brain under Different Anesthetic Conditions, Metabolites 11 (2021).
[44] S. Kishimoto, J.R. Brendert, D.R. Crooks, S. Matsumoto, T. Seki, N. Oshima, H. Merkle, P.H. Lin, G. Reed, A.P. Chen, J.H. Ardenkjaer-Larsen, J. Munasinghe, K. Saito, K. Yamamoto, P.L. Choyke, J. Mitchell, A.N. Lane, T.W.M. Fan, W.M. Linehan, M.C. Krishna, Imaging of glucose metabolism by ^{13}C-MRI distinguishes pancreatic cancer subtypes in mice, Elife 8 (2019) e46312.
[45] S. Walker-Samuel, R. Ramasawmy, F. Torrealdea, M. Rega, V. Rajkumar, S.P. Johnson, S. Richardson, M. Gonçalves, H.G. Parkes, E. Arstad, D.L. Thomas, R.B. Pedley, M.F. Lythgoe, X. Golay, *In vivo* imaging of glucose uptake and metabolism in tumors, Nat Med 19 (2013) 1067–1072.
[46] R.A. Gatenby, R.J. Gillies, Why do cancers have high aerobic glycolysis?, Nat Rev Cancer 4 (2004) 891–899
[47] R.L. Hesketh, J. Wang, A.J. Wright, D.Y. Lewis, A.E. Denton, R. Grenfell, J.L. Miller, R. Bielik, M. Gehrung, M. Fala, S. Ros, B. Xie, D.E. Hu, K.M. Brindle, Magnetic Resonance Imaging Is More Sensitive Than PET for Detecting Treatment-Induced Cell Death-Dependent Changes in Glycolysis, Cancer Res 79 (2019) 3557–3569.
[48] A. Bertoldo, J. Price, C. Mathis, S. Mason, D. Holt, C. Kelley, C. Cobelli, D.E. Kelley, Quantitative assessment of glucose transport in human skeletal muscle: dynamic positron emission tomography imaging of [O-methyl-^{11}C]3-O-methyl-D-glucose, J Clin Endocrinol Metab 90 (2005) 1752–1759.
[49] M. Rivlin, G. Navon, CEST MRI of 3-O-methyl-D-glucose on different breast cancer models, Magn Reson Med 79 (2018) 1061–1069.
[50] B. Hartmann, M. Müller, L. Seyler, T. Bäuerle, T. Wilferth, N. Avdievitch, L. Ruhm, A. Henning, A. Lesiv, P. Ivashkin, M. Uder, A.M. Nagel, Feasibility of deuterium magnetic resonance spectroscopy of 3-O-Methylglucose at 7 Tesla, PLoS One 16 (2021) e0252935.
[51] B. Lanz, L. Xin, P. Millet, R. Gruetter, *In vivo* quantification of neuro-glial metabolism and glial glutamate concentration using ^{1}H-[^{13}C] MRS at 14.1T, J. Neurochem. 128 (2014) 125–139.
[52] I. Grassi, C. Nanni, V. Allegri, J.J. Morigi, G.C. Montini, P. Castellucci, S. Fanti, The clinical use of PET with ^{11}C-acetate, Am J Nucl Med Mol Imaging 2 (2012) 33–47.
[53] D.Y. Lewis, J. Boren, G.L. Shaw, R. Bielik, A. Ramos-Montoya, T.J. Larkin, C.P. Martins, D.E. Neal, D. Soloviev, K.M. Brindle, Late Imaging with [1-^{11}C]Acetate Improves Detection of Tumor Fatty Acid Synthesis with PET, J Nucl Med 55 (2014) 1144–1149.
[54] I.M. Brereton, M.G. Irving, J. Field, D.M. Doddrell, Preliminary studies on the potential of *in vivo* deuterium NMR spectroscopy, Biochem. Biophys. Res. Commun. 137 (1986) 579–584.
[55] J.A. Bastiaansen, T. Cheng, H. Lei, R. Gruetter, A. Comment, Direct noninvasive estimation of myocardial tricarboxylic acid cycle flux in vivo using hyperpolarized ^{13}C magnetic resonance, J Mol Cell Cardiol 87 (2015) 129–137.
[56] J.A. Bastiaansen, M.E. Merritt, A. Comment, Real time measurement of myocardial substrate selection *in vivo* using hyperpolarized ^{13}C magnetic resonance, J. Cardiovasc. Magn. Reson. 17 (Suppl. 1) (2015) O15.
[57] D.S. Wishart, C. Knox, A.C. Guo, R. Eisner, N. Young, B. Gautam, D.D. Hau, N. Psychogios, E. Dong, S. Bouatra, R. Mandal, I. Sinelnikov, J. Xia, L. Jia, J.A. Cruz, E. Lim, C.A. Sobsey, S. Shrivastava, P. Huang, P. Liu, L. Fang, J. Peng, R. Fradette, D. Cheng, D. Tzur, M. Clements, A. Lewis, A. De Souza, A. Zuniga, M. Dawe, Y. Xiong, D. Clive, R. Greiner, A. Nazyrova, R. Shaykhutdinov, L. Li, H.J. Vogel, I. Forsythe, HMDB: a knowledgebase for the human metabolome, Nucl. Acids Res 37 (2009) D603–D610.
[58] J. van den Hoff, W. Burchert, H.G. Wolpers, G.J. Meyer, H. Hundeshagen, A kinetic model for cardiac PET with [1-carbon-11]-acetate, J Nucl Med 37 (1996) 521–529.
[59] K. Glunde, Z.M. Bhujwalla, S.M. Ronen, Choline metabolism in malignant transformation, Nat Rev Cancer 11 (2011) 835–848.
[60] R. Katz-Brull, R. Margalit, P. Bendel, H. Degani, Choline metabolism in breast cancer; ^{2}H-, ^{13}C- and ^{31}P-NMR studies of cells and tumors, MAGMA 6 (1998) 44–52.
[61] A. Veltien, J. van Asten, N. Ravichandran, R.A. de Graaf, H.M. De Feyter, E. Oosterwijk, A. Heerschap, Simultaneous Recording of the Uptake and Conversion of Glucose and Choline in Tumors by Deuterium Metabolic Imaging, Cancers 13 (2021) 4034.
[62] H.M. De Feyter, M.A. Thomas, K.L. Ip, K.I. Behar, R.A. de Graaf, Delayed mapping of ^{2}H-labeled choline using Deuterium Metabolic Imaging (DMI) reveals active choline metabolism in rat glioblastoma, in: In Proceedings of the International Society of Magnetic Resonance in Medicine. , 2021, pp. 0016.
[63] C. Gabellieri, S. Reynolds, A. Lavie, G.S. Payne, M.O. Leach, T.R. Eykyn, Therapeutic Target Metabolism Observed Using Hyperpolarized ^{15}N Choline, J. Am. Chem. Soc. 130 (2008) 4598–4599.
[64] C. Cudalbu, A. Comment, F. Kurdzesau, R.B. van Heeswijk, K. Uffmann, S. Jannin, V. Denisov, D. Kirik, R. Gruetter, Feasibility of *in vivo* ^{15}N MRS detection of hyperpolarized ^{15}N labeled choline in rats, PCCP 12 (2010) 5818–5823.
[65] L.J. Friesen-Waldner, T.P. Wade, K. Thind, A.P. Chen, J.M. Gomori, J. Sosna, C.A. McKenzie, R. Katz-Brull, Hyperpolarized choline as an MR imaging molecular probe: Feasibility of *in vivo* imaging in a rat model, J. Magn. Reson. Imaging 41 (2015) 917–923.
[66] T. Hara, N. Kosaka, N. Shinoura, T. Kondo, PET imaging of brain tumor with [methyl-^{11}C]choline, J Nucl Med 38 (1997) 842–847.
[67] S.N. Reske, N.M. Blumstein, B. Neumaier, H.W. Gottfried, F. Finsterbusch, D. Kocot, P. Möller, G. Glatting, S. Perner, Imaging prostate cancer with ^{11}C-choline PET/CT, J Nucl Med 47 (2006) 1249–1254.
[68] K.B. Contractor, L.M. Kenny, J. Stebbing, A. Al-Nahhas, C. Palmieri, D. Sinnett, J. S. Lewis, K. Hogben, S. Osman, S. Shousha, C. Lowdell, R.C. Coombes, E.O. Aboagye, [^{11}C]choline positron emission tomography in estrogen receptor-positive breast cancer, Clin Cancer Res 15 (2009) 5503–5510.
[69] G. Batsios, C. Taglang, M. Tran, N. Stevers, C. Barger, A.M. Gillespie, S.M. Ronen, J.F. Costello, P. Viswanath, Deuterium Metabolic Imaging Reports on TERT Expression and Early Response to Therapy in Cancer, Clin Cancer Res 28 (2022) 3526–3536.
[70] K.R. Keshari, D.M. Wilson, Chemistry and biochemistry of ^{13}C hyperpolarized magnetic resonance using dynamic nuclear polarization, Chem. Soc. Rev. 43 (2014) 1627–1659.
[71] A. Comment, M.E. Merritt, Hyperpolarized magnetic resonance as a sensitive detector of metabolic function, Biochemistry 53 (2014) 7333–7357.
[72] K.M. Brindle, Imaging Metabolism with Hyperpolarized ^{13}C-Labeled Cell Substrates, J. Am. Chem. Soc. 137 (2015) 6418–6427.
[73] S.J. Nelson, J. Kurhanewicz, D.B. Vigneron, P.E. Larson, A.L. Harzstark, M. Ferrone, M. van Criekinge, J.W. Chang, R. Bok, I. Park, G. Reed, L. Carvajal, E.J. Small, P. Munster, V.K. Weinberg, J.H. Ardenkjaer-Larsen, A.P. Chen, R.E. Hurd, L.I. Odegardstuen, F.J. Robb, J. Tropp, J.A. Murray, Metabolic imaging of patients with prostate cancer using hyperpolarized [1-^{13}C]pyruvate, Sci Transl Med 5 (2013) 198ra108.
[74] J.T. Grist, M.A. McLean, F. Riemer, R.F. Schulte, S.S. Deen, F. Zaccagna, R. Woitek, C.J. Daniels, J.D. Kaggie, T. Matys, I. Patterson, R. Slough, A.B. Gill, A. Chhabra, R. Eichenberger, M.C. Laurent, A. Comment, J.H. Gillard, A.J. Coles, D. J. Tyler, I. Wilkinson, B. Basu, D.J. Lomas, M.J. Graves, K.M. Brindle, F.A. Gallagher, Quantifying normal human brain metabolism using hyperpolarized [1-^{13}C]pyruvate and magnetic resonance imaging, Neuroimage 189 (2019) 171–179.
[75] C.Y. Lee, H. Soliman, B.J. Geraghty, A.P. Chen, K.A. Connelly, R. Endre, W.J. Perks, C. Heyn, S.E. Black, C.H. Cunningham, Lactate topography of the human brain using hyperpolarized ^{13}C-MRI, Neuroimage 204 (2020).
[76] C.H. Cunningham, J.Y. Lau, A.P. Chen, B.J. Geraghty, W.J. Perks, I. Roifman, G.A. Wright, K.A. Connelly, Hyperpolarized ^{13}C Metabolic MRI of the Human Heart: Initial Experience, Circ Res 119 (2016) 1177–1182.
[77] O.J. Rider, A. Apps, J. Miller, J.Y.C. Lau, A.J.M. Lewis, M.A. Peterzan, M.S. Dodd, A.Z. Lau, C. Trumper, F.A. Gallagher, J.T. Grist, K.M. Brindle, S. Neubauer, D.J. Tyler, Noninvasive *In Vivo* Assessment of Cardiac Metabolism in the Healthy and Diabetic Human Heart Using Hyperpolarized ^{13}C MRI, Circ Res 126 (2020) 725–736.
[78] F.A. Gallagher, R. Woitek, M.A. McLean, A.B. Gill, R. Manzano Garcia, E. Provenzano, F. Riemer, J. Kaggie, A. Chhabra, S. Ursprung, J.T. Grist, C.J. Daniels, F. Zaccagna, M.C. Laurent, M. Locke, S. Hilborne, A. Frary, T. Torheim, C. Boursnell, A. Schiller, I. Patterson, R. Slough, B. Carmo, J. Kane, H. Biggs, E. Harrison, S.S. Deen, A. Patterson, T. Lanz, Z. Kingsbury, M. Ross, B. Basu, R. Baird, D.J. Lomas, E. Sala, J. Wason, O.M. Rueda, S.F 117 (2020) 2092–2098, Graves, J.E. Abraham, F.J. Gilbert, C. Caldas, K.M. Brindle, Imaging breast cancer using hyperpolarized carbon-13 MRI, Proc Natl Acad Sci U S A.
[79] R. Woitek, M.A. McLean, S. Ursprung, O.M. Rueda, R. Manzano Garcia, M.J. Locke, L. Beer, G. Baxter, L. Rundo, E. Provenzano, J. Kaggie, A. Patterson, A. Frary, J. Field-Rayner, V. Papalouka, J. Kane, A.J.V. Benjamin, A.B. Gill, A.N. Priest, D.Y. Lewis, R. Russell, A. Grimmer, B. White, B. Latimer-Bowman, I. Patterson, A. Schiller, B. Carmo, R. Slough, T. Lanz, J. Wason, R.F. Schulte, S.F. Chin, M.J. Graves, F.J. Gilbert, J.E. Abraham, C. Caldas, K.M. Brindle, E. Sala, F.A. Gallagher, Hyperpolarized Carbon-13 MRI for Early Response Assessment of Neoadjuvant Chemotherapy in Breast Cancer Patients, Cancer Res 81 (2021) 6004–6017.
[80] I. Park, P.E.Z. Larson, J.W. Gordon, L. Carvajal, H.Y. Chen, R. Bok, M. Van Criekinge, M. Ferrone, J.B. Slater, D. Xu, J. Kurhanewicz, D.B. Vigneron, S. Chang, S.J. Nelson, Development of methods and feasibility of using hyperpolarized carbon-13 imaging data for evaluating brain metabolism in patient studies, Magn Reson Med 80 (2018) 864–873.
[81] V.Z. Miloushev, K.L. Granlund, R. Boltyanskiy, S.K. Lyashchenko, L.M. DeAngelis, I.K. Mellinghoff, C.W. Brennan, V. Tabar, T.J. Yang, A.I. Holodny, R.E. Sosa, Y.W. Guo, A.P. Chen, J. Tropp, F. Robb, K.R. Keshari, Metabolic Imaging of the Human Brain with Hyperpolarized ^{13}C Pyruvate Demonstrates

^{13}C Lactate Production in Brain Tumor Patients, Cancer Res 78 (2018) 3755–3760.
[82] A.W. Autry, J.W. Gordon, H.Y. Chen, M. LaFontaine, R. Bok, M. Van Criekinge, J. B. Slater, L. Carvajal, J.E. Villanueva-Meyer, S.M. Chang, J.L. Clarke, J.M. Lupo, D. Xu, P.E.Z. Larson, D.B. Vigneron, Y. Li, Characterization of serial hyperpolarized ^{13}C metabolic imaging in patients with glioma, Neuroimage Clin 27 (2020).
[83] F. Zaccagna, M.A. McLean, J.T. Grist, J. Kaggie, R. Mair, F. Riemer, R. Woitek, A. B. Gill, S. Deen, C.J. Daniels, S. Ursprung, R.F. Schulte, K. Allinson, A. Chhabra, M.-C. Laurent, M. Locke, A. Frary, S. Hilborne, I. Patterson, B.D. Carmo, R. Slough, I. Wilkinson, B. Basu, J. Wason, J.H. Gillard, T. Matys, C. Watts, S.J. Price, T. Santarius, M.J. Graves, S. Jefferies, K.M. Brindle, F.A. Gallagher, Imaging Glioblastoma Metabolism by Using Hyperpolarized [1-^{13}C]Pyruvate Demonstrates Heterogeneity in Lactate Labeling: A Proof of Principle Study, Radiology: Imaging Cancer 4 (2022).
[84] H. Stødkilde-Jørgensen, C. Laustsen, E.S.S. Hansen, R. Schulte, J.H. Ardenkjaer-Larsen, A. Comment, J. Frøkiaer, S. Ringgaard, L.B. Bertelsen, M. Ladekarl, B. Weber, Pilot Study Experiences With Hyperpolarized [1-^{13}C]pyruvate MRI in Pancreatic Cancer Patients, J Magn Reson Imaging 51 (2020) 961–963.
[85] S. Ursprung, R. Woitek, M.A. McLean, A.N. Priest, M. Crispin-Ortuzar, C.R. Brodie, A.B. Gill, M. Gehrung, L. Beer, A.C.P. Riddick, J. Field-Rayner, J.T. Grist, S.S. Deen, F. Riemer, J.D. Kaggie, F. Zaccagna, J.A.G. Duarte, M.J. Locke, A. Frary, T.F. Aho, J.N. Armitage, R. Casey, I.A. Mendichovszky, S.J. Welsh, T. Barrett, M.J. Graves, T. Eisen, T.J. Mitchell, A.Y. Warren, K.M. Brindle, E. Sala, G.D. Stewart, F.A. Gallagher, Hyperpolarized ^{13}C-Pyruvate Metabolism as a Surrogate for Tumor Grade and Poor Outcome in Renal Cell Carcinoma-A Proof of Principle Study, Cancers (Basel) 14 (2022) 335.
[86] N. Sushentsev, M.A. McLean, A.Y. Warren, A.J.V. Benjamin, C. Brodie, A. Frary, A.B. Gill, J. Jones, J.D. Kaggie, B.W. Lamb, M.J. Locke, J.L. Miller, I.G. Mills, A.N. Priest, F.J.L. Robb, N. Shah, R.F. Schulte, M.J. Graves, V.J. Gnanapragasam, K.M. Brindle, T. Barrett, F.A. Gallagher, Hyperpolarised ^{13}C-MRI identifies the emergence of a glycolytic cell population within intermediate-risk human prostate cancer, Nat Commun 13 (2022) 466.
[87] I. de Kouchkovsky, H.Y. Chen, M.A. Ohliger, Z.J. Wang, R.A. Bok, J.W. Gordon, P. E.Z. Larson, M. Frost, K. Okamoto, M.R. Cooperberg, J. Kurhanewicz, D.B. Vigneron, R. Aggarwal, Hyperpolarized [1-^{13}C]-Pyruvate Magnetic Resonance Imaging Detects an Early Metabolic Response to Immune Checkpoint Inhibitor Therapy in Prostate Cancer, Eur Urol 81 (2022) 219–221.
[88] Z.J. Wang, M.A. Ohliger, P.E.Z. Larson, J.W. Gordon, R.A. Bok, J. Slater, J.E. Villanueva-Meyer, C.P. Hess, J. Kurhanewicz, D.B. Vigneron, Hyperpolarized ^{13}C MRI: State of the Art and Future Directions, Radiology 291 (2019) 273–284.
[89] J. Kurhanewicz, D.B. Vigneron, J.H. Ardenkjaer-Larsen, J.A. Bankson, K. Brindle, C.H. Cunningham, F.A. Gallagher, K.R. Keshari, A. Kjaer, C. Laustsen, D.A. Mankoff, M.E. Merritt, S.J. Nelson, J.M. Pauly, P. Lee, S. Ronen, D.J. Tyler, S.S. Rajan, D.M. Spielman, L. Wald, X. Zhang, C.R. Malloy, R. Rizi, Hyperpolarized ^{13}C MRI: Path to Clinical Translation in Oncology, Neoplasia 21 (2019) 1–16.
[90] T.H. Witney, M.I. Kettunen, K.M. Brindle, Kinetic modeling of hyperpolarized ^{13}C label exchange between pyruvate and lactate in tumor cells, J Biol Chem 286 (2011) 24572–24580.
[91] I. de Kouchkovsky, H.Y. Chen, M.A. Ohliger, Z.J. Wang, R.A. Bok, J.W. Gordon, P. E.Z. Larson, M. Frost, K. Okamoto, M.R. Cooperberg, J. Kurhanewicz, D.B. Vigneron, R. Aggarwal, Hyperpolarized 1–^{13}C]-Pyruvate Magnetic Resonance Imaging Detects an Early Metabolic Response to Immune Checkpoint Inhibitor Therapy in Prostate Cancer, Eur Urol 81 (2022) 219–221.
[92] J.M. Park, D.M. Spielman, S. Josan, T. Jang, M. Merchant, R.E. Hurd, D. Mayer, L. D. Recht, Hyperpolarized ^{13}C-lactate to ^{13}C-bicarbonate ratio as a biomarker for monitoring the acute response of anti-vascular endothelial growth factor (anti-VEGF) treatment, NMR Biomed 29 (2016) 650–659.
[93] J.D. Kaggie, A.S. Khan, T. Matys, R.F. Schulte, M.J. Locke, A. Grimmer, A. Frary, I. H. Menih, E. Latimer, M.J. Graves, M.A. McLean, F.A. Gallagher, Deuterium metabolic imaging and hyperpolarized ^{13}C-MRI of the normal human brain at clinical field strength reveals differential cerebral metabolism, Neuroimage 257 (2022).
[94] F. Hesse, A.J. Wright, V. Somai, F. Bulat, F. Kreis, K.M. Brindle, Imaging Glioblastoma Response to Radiotherapy Using ^{2}H Magnetic Resonance Spectroscopy Measurements of Fumarate Metabolism, Cancer Res 82 (2022) 3622–3633.
[95] F.A. Gallagher, M.I. Kettunen, D.E. Hu, P.R. Jensen, R.I. Zandt, M. Karlsson, A. Gisselsson, S.K. Nelson, T.H. Witney, S.E. Bohndiek, G. Hansson, T. Peitersen, M.H. Lerche, K.M. Brindle, Production of hyperpolarized [1,4–$^{13}C_2$]malate from [1,4–$^{13}C_2$]fumarate is a marker of cell necrosis and treatment response in tumors, Proc Natl Acad Sci U S A 106 (2009) 19801–19806.
[96] T.H. Witney, M.I. Kettunen, D.E. Hu, F.A. Gallagher, S.E. Bohndiek, R. Napolitano, K.M. Brindle, Detecting treatment response in a model of human breast adenocarcinoma using hyperpolarised [1-^{13}C]pyruvate and [1,4–$^{13}C_2$]fumarate, Br J Cancer 103 (2010) 1400–1406.
[97] S.E. Bohndiek, M.I. Kettunen, D.-E. Hu, K.M. Brindle, Hyperpolarized ^{13}C Spectroscopy Detects Early Changes in Tumor Vasculature and Metabolism after VEGF Neutralization, Cancer Res. 72 (2012) 854–864.
[98] J.J. Miller, A.Z. Lau, P.M. Nielsen, G. McMullen-Klein, A.J. Lewis, N.R. Jespersen, V. Ball, F.A. Gallagher, C.A. Carr, C. Laustsen, H.E. Bøtker, D.J. Tyler, M.A. Schroeder, Hyperpolarized [1,4-$^{13}C_2$]Fumarate Enables Magnetic Resonance-Based Imaging of Myocardial Necrosis, JACC: Cardiovasc. Imag. 11 (2018) 1594–1606.
[99] M.R. Clatworthy, M.I. Kettunen, D.E. Hu, R.J. Mathews, T.H. Witney, B.W. Kennedy, S.E. Bohndiek, F.A. Gallagher, L.B. Jarvis, K.G. Smith, K.M. Brindle, Magnetic resonance imaging with hyperpolarized [1,4–$^{13}C_2$]fumarate allows detection of early renal acute tubular necrosis, Proc. Natl. Acad. Sci. USA 109 (2012) 13374–13379.
[100] F. Hesse, A.J. Wright, F. Bulat, V. Somai, F. Kreis, K.M. Brindle, Deuterium MRSI of tumor cell death *in vivo* following oral delivery of ^{2}H-labeled fumarate, Magn. Reson. Med. 88 (2022) 2014–2020.
[101] O. Bodansky, H. Gold, W. Zahm, The toxicity and laxative action of sodium fumarate, J. Am. Pharm. Assoc. 31 (1942) 1–8.